Revision 1

Experimental Constraints on Fluid-Rock Reactions During Incipient Serpentinization of Harzburgite

Frieder Klein[1*], Niya G. Grozeva[2], Jeffrey S. Seewald[1], Thomas M. McCollom[3], Susan E. Humphris[4], Bruce Moskowitz[5], Thelma S. Berquó[6], and Wolf-Achim Kahl[7]

[1] *Department of Marine Chemistry and Geochemistry, Woods Hole Oceanographic Institution, Woods Hole, MA 02543, USA*

[2]*Massachusetts Institute of Technology/Woods Hole Oceanographic Institution Joint Program in Oceanography, Cambridge, MA 02139, USA*

[3]*Laboratory for Atmospheric and Space Physics, Campus Box 392, University of Colorado, Boulder, CO 80309-0392, USA*

[4]*Department of Geology and Geophysics, Woods Hole Oceanographic Institution, Woods Hole, MA 02543, USA*

[5]*Department of Earth Sciences, and Institute for Rock Magnetism, University of Minnesota, Minneapolis, MN 55455, USA*

[6]*Department of Physics, Concordia College, Moorhead, MN 56562, USA*

[7] *Geosciences Department, University of Bremen, Bremen, 28359, Germany*

[*] *corresponding author*

ABSTRACT

The exposure of mantle peridotite to water at crustal levels leads to a cascade of interconnected dissolution-precipitation and reduction-oxidation reactions - a process referred to as serpentinization. These reactions have major implications for microbial life through the provision of hydrogen (H_2). To simulate incipient serpentinization under well-constrained conditions, we reacted cm-sized pieces of uncrushed harzburgite with chemically modified seawater at 300°C and 35 MPa for ca. 1.5 years (13441 hours), monitored changes in fluid chemistry over time, and examined the secondary mineralogy at the termination of the experiment. Approximately 4 mol % of the protolith underwent alteration forming serpentine, accessory magnetite, chlorite, and traces of calcite and heazlewoodite. Alteration textures bear remarkable similarities to those found in partially serpentinized abyssal peridotites. Neither brucite nor talc precipitated during the experiment. Given that the starting material contained ~4 times more olivine than orthopyroxene on a molar basis, mass balance requires that dissolution of orthopyroxene was significantly faster than dissolution of olivine. Coupled mass transfer of dissolved Si, Mg, and H^+ between olivine and orthopyroxene reaction fronts was driven by steep activity gradients and facilitated the precipitation of serpentine. Hydrogen was released in significant amounts throughout the entire experiment; however, the H_2 release rate decreased with time. Serpentinization consumed water but did not release significant amounts of dissolved species (other than H_2) suggesting that incipient hydration reactions involved a volume increase of ~40%. The reduced access of water to fresh olivine surfaces due to filling of

fractures and coating of primary minerals with alteration products led to decreased rates of serpentinization and H_2 release. While this concept might seem at odds with completely serpentinized seafloor peridotites, reaction-driven fracturing offers an intriguing solution to the seemingly self-limiting nature of serpentinization. Indeed, the reacted sample revealed a number of textural features diagnostic of incipient reaction-driven fracturing. We conclude that fracturing must have far reaching impacts on the rates of serpentinization and H_2 release in peridotite-hosted hydrothermal systems.

Keywords: *serpentinization, phase relations, reaction rates, reaction pathways, fracturing, hydrogen, hydrothermal experiment*

INTRODUCTION

Serpentinization reactions play a prominent role in a wide range of geophysical, geochemical, and biological processes on Earth, including seafloor spreading, cycling of water, carbon, and sulfur, abiotic synthesis of organic compounds, and chemosynthesis (Alt et al., 2013; Escartín et al., 1997; Foustoukos and Seyfried, 2004; Lang et al., 2010; Schrenk et al., 2013; Schwarzenbach et al., 2013; Seewald et al., 2006). Serpentinization reactions directly impact the mechanical properties, magnetic signatures, densities, electrical conductivities, and trace element contents of ultramafic rocks (Coleman, 1971; Deschamps et al., 2011; Escartin et al., 2001; Iyer et al., 2008; Jöns et al., 2010; Kelemen and Hirth, 2012; Kodolanyi et al., 2012; Maffione et al., 2014; Oufi et al., 2002; Paulick et al., 2006;

Plümper et al., 2012; Reynard et al., 2011; Stesky and Brace, 1973; Toft et al., 1990). A key result of serpentinization is the release of H_2 and the creation of chemical environments that are sufficiently reducing to stabilize native metals and alloys (Chamberlain et al., 1965) and reduce CO_2 (Foustoukos and Seyfried, 2004; Horita and Berndt, 1999; McCollom and Seewald, 2001). Moreover, the release of H_2 can also provide chemolithoautotrophic microorganisms with chemical energy (Brazelton et al., 2012; Perner et al., 2007; Schrenk et al., 2013).

The mechanisms controlling the release of H_2 can be studied in active and fossil hydrothermal systems, using laboratory experiments, and theoretical models. Field investigations have highlighted numerous factors that influence the composition of hydrothermal fluids, such as rock composition, temperature, pressure, water-to-rock mass ratio, degassing of magmatic volatiles, fluid mixing, phase separation, stable and metastable fluid-mineral equilibria, reaction kinetics, porosity, permeability, and biological activity (e.g., Alt and Shanks, 1998; Früh-Green et al., 2003; Ludwig et al., 2006; Pester et al., 2012; Proskurowski et al., 2006; Schmidt et al., 2007). Because fluids can integrate a number of individual reactions involving different rock types along the flow path (Nakamura et al., 2009), chemical processes during fluid-rock interactions often remain difficult to reconstruct by field studies alone.

Thermodynamic modeling has been used to augment field studies, in particular to quantify heterogeneous equilibria of complex multi-component systems (Alt and Shanks, 2003; Bach et al., 2013; Jöns et al., 2010; Klein et al., 2013; Seyfried et al., 2011; Shock and Canovas, 2010; Sleep et al., 2004; Wetzel and Shock,

2000). However, thermodynamic models rely on field observations or laboratory experiments to constrain kinetically-limited, metastable, and/or permeability-limited reactions. Laboratory experiments offer the advantage that stable and metastable phase equilibria, reaction pathways, reaction rates, and many other parameters can be studied under well-constrained temperature, pressure, and compositional conditions. Powdered reactants are commonly used in serpentinization experiments to allow reactions to proceed on laboratory timescales (e.g., Klein and McCollom, 2013; Malvoisin et al., 2012b; Seyfried and Dibble, 1980). However, an inherent drawback of powdered reactants is that effects related to changes in permeability and porosity – key properties in regulating fluid access to primary mineral surfaces (Godard et al., 2013) – cannot be studied.

An intimately linked and still debated question is whether serpentinization is an isovolumetric process associated with mass transfer or whether it occurs via simple hydration that requires a volume increase. Isovolumetric serpentinization implies open system behavior and the removal of Mg, Fe, and Si to accommodate the uptake of water. Thayer (1966) argued that the preservation of primary textures such as euhedral olivine pseudomorphs indicates volume-for-volume replacement and open system behavior (cf. Velbel, 2014). In contrast, Hostetler et al. (1966) and Page (1967) did not find any field evidence for large-scale removal of Mg or Si. Isochemical serpentinization (apart from the addition of water) involves large volume increases, which, depending on the protolith composition can be up to 53% (O'Hanley, 1992). The resulting decrease in permeability has led some to infer that serpentinization represents a self-sealing mechanism (Lister, 1974).

The concept that serpentinization results in decreased permeability is in contrast to the high degrees of serpentinization observed in orogenic, ophiolitic, and abyssal peridotites (Bodinier and Godard, 2007; Dick, 1989). An intriguing explanation for this observation is persistent reaction-driven fracturing, which may create new and reactivate existing pathways for fluid transport (Kelemen and Hirth, 2012; Plümper et al., 2012; Rouméjon and Cannat, 2014). Some laboratory experiments suggest that serpentinization at elevated temperatures is a fast process on geological timescales (Malvoisin et al., 2012a; Martin and Fyfe, 1970; Wegner and Ernst, 1983), limited only by water access to primary mineral surfaces (Macdonald and Fyfe, 1985; Malvoisin and Brunet, 2014). While the use of powdered starting materials in laboratory serpentinization experiments has provided valuable insight by allowing reactions to go to completion, this approach does not permit testing of whether serpentinization is a self-sealing process (Lister, 1974), or whether serpentinization can go to completion via thermal, tectonic, and reaction-driven fracturing (Plümper et al., 2012, Rouméjon and Cannat, 2014). Moreover, it remains unclear how the putative self-sealing nature of serpentinization or fracturing affects rates of mineral dissolution and H_2 release.

With only a few exceptions (e.g., Craddock et al., 2013), abyssal peridotites are strongly to completely serpentinized (40-100%), making it difficult to study the earliest stages of serpentinization in seafloor environments. We have conducted an experimental study to investigate the onset of mineral replacement reactions and associated changes in fluid chemistry under well-constrained conditions. We reacted uncrushed harzburgite and modified seawater, monitored changes in fluid

chemistry over time, and examined solid reaction products in their textural context. In addition to providing new insights into reactions taking place during the earliest stages of serpentinization (cf., Beard et al., 2009; Godard et al., 2013), the results suggest that H_2 release rates are constrained by water access to primary minerals, further supporting the idea that continuous fracturing is required for serpentinization to go to completion.

METHODS and MATERIALS

Experimental setup and analytical techniques – The experiment was carried out in a flexible-cell hydrothermal apparatus (Seyfried et al., 1979) consisting of a gold bag with a titanium closure piece, exit tube, and sampling valve. All Ti surfaces in contact with the fluid were oxidized in air at 400 °C prior to the experiment to prevent artificial H_2 release. The flexible reaction cell is enclosed in a stainless steel pressure-containment vessel filled with water, which acts as the pressure medium. The flexible gold bag permits external control of pressure and the elimination of a vapor headspace during the experiment. The titanium sample valve allows periodic removal of fluid during the experiment for chemical characterization.

After loading the reaction cell with 18.19 g of harzburgite and 43.15 g of evolved seawater (compositional details of starting materials are presented below), the reaction cell was pressurized to 35MPa and heated to 300°C. When the desired experimental conditions were reached, the system was allowed to react for 13441 h.

Several aliquots (0.3-0.6 g each, ~3 g of fluid in total per sampling event) of fluid were taken in gas-tight glass syringes on six occasions during the experiment.

Quantitative analysis of dissolved H_2 was performed using a gas chromatograph equipped with a thermal conductivity detector. Dissolved cations were analyzed by inductively coupled plasma mass spectrometry (Mg) and ion chromatography (Na, K, Ca). Estimated uncertainties are 2% for Mg, 3% for Na and K, and 5% for Ca. Dissolved Si was measured spectrophotometrically using the heteropoly-blue method at a wavelength of 815nm. The estimated uncertainty was 5%. The pH (25°C) was measured using a micro-combination electrode. The uncertainty was ca. 0.1 unit of the reported value.

Polished thin sections of the solid starting material and experimental reaction products were prepared in oil at High Mesa Petrographics, Los Alamos, NM to avoid oxidation of Fe(II)-bearing minerals and dissolution of water-soluble phases. Thin sections were examined optically in transmitted and reflected light with a petrographic microscope. Backscattered electron images of thin sections and rock chips were taken with a Hitachi TM3000 scanning electron microscope, the low-vacuum mode of which permits analysis without carbon coating the sample. Element distribution mapping was conducted with a Bruker Quantax 70 energy dispersive X-ray spectrometer coupled to the scanning electron microscope. Mineral compositions were quantified with a JEOL JXA-8530F 'HyperProbe' Field-Emission Electron Probe Microanalyzer (Yale University) operated at 15 kV acceleration voltage and 20nA beam current. The beam was fully focused for primary silicates and sulfides, but was set to 5-15 μm in diameter for all other phases to avoid beam damage. Counting times for all elements were 20 seconds except for F, which was analyzed for 120 seconds. Raw data were corrected using

the CITZAF method (Armstrong, 1995). The accuracy and precision of electron microprobe analysis was ca. 1%.

Thin sections and rock chips were analyzed with a Horiba LabRAM HR confocal Raman spectrometer equipped with a 17 mW 633 nm HeNe laser, an astigmatic flat field spectrograph with a focal length of 800 mm, and a multichannel air-cooled (-70 °C) CCD detector. For thin sections, individual spectra were recorded using a 100x objective with a numerical aperture of 0.9. A grating with 600 grooves / mm was used for identification of minerals. A confocal hole diameter of 100 µm was chosen for most analyses. Spectra were collected for 5 seconds with 3-5 accumulations between 100 cm^{-1} and 1300 cm^{-1}.

Magnetic susceptibilities (K) and volumes of solids were measured with a Bartington MS2B sensor and a Micromeritics AccuPyc II He-pycnometer. The calibration accuracy for both instruments was 1%. Loss on ignition (LOI) and bulk rock chemical X-ray fluorescence analysis of powders were carried out at the Peter Hooper GeoAnalytical Lab at Washington State University, Pullman, WA. The estimated uncertainty for major elements is on the order of 1%. To quantify the amount of magnetite present and the distribution, coordination, and oxidation state of iron in secondary minerals, Mössbauer spectroscopic and magnetization measurements were conducted at the Institute for Rock Magnetism at the University of Minnesota (see Klein et al., 2009 for more detailed information).

Starting materials – A peridotite xenolith from the Eifel Volcanic Field (Meerfelder Maar, Eifel Volcanic Field, Germany) was used for this study to avoid any pre-

existing serpentinization of the starting material (Figs. 1, 2). Mass balancing the bulk major element composition of the starting material as determined with X-ray fluorescence and electron microprobe analysis (Tables 1, 2) suggests that the peridotite can be classified as a harzburgite consisting of olivine (~70 wt.%), orthopyroxene (~25 wt.%), clinopyroxene (~4 wt.%), Cr-spinel (~0.9 wt.%), and traces (<0.1 wt.%) of amphibole, glass, and primary sulfides. These mineral abundances are consistent with those estimated from optical thin section and X-ray microtomography (μ-CT) image analysis. However, mineral proportions can vary on a thin section scale (Fig. 1). All primary silicates are relatively uniform in composition and do not show any core-to rim variation as determined from electron microprobe analysis (Table 2). The harzburgite is moderately fractured (Figs. 1 and 2), most likely due to decompression and thermal relaxation during rapid ascent of the xenolith (cf. Klügel and Klein, 2006). Fracture widths range from < 1µm to 10µm (Fig. 2).

Olivine, orthopyroxene, and clinopyroxene have a Mg# ((mol MgO/(MgO+FeO)x100) of ~ 91 and NiO, MnO, Al_2O_3, Cr_2O_3, and CaO contents typical for these minerals in mantle peridotite (Table 2). Rare amphibole is approximately of pargasitic composition, has a Mg# of 89, and has slightly elevated contents of K_2O and Cr_2O_3 compared with its ideal end-member. Chromian spinel compositions were not determined as detailed thin section petrography of the reaction products revealed that it did not undergo reaction during the experiment. Pentlandite contains low concentrations of Co (0.6-0.7 wt.%) and Cu (0.1-0.2 wt.%), and Ni is enriched relative to Fe. The empirical formula of pentlandite in the starting material

is $Ni_{4.9}Fe_{4.1}S_8$. Pyrrhotite was analyzed semi-quantitatively with energy-dispersive spectroscopy and is approximately of stoichiometric composition.

Olivine and orthopyroxene are anhedral to subhedral with grain diameters ranging between 0.3 mm and 3.0 mm (average of 1.0 mm) and 0.5 mm and 3.0 mm (average of 0.8 mm), respectively (Fig. 1). Grain diameters of anhedral to euhedral clinopyroxene range between 0.05 mm and 1.0 mm (average of 0.4 mm). Weakly pleochroic anhedral to subhedral amphibole, 0.1-0.2 mm in diameter, occurs in association with Cr-spinel. It remains unclear whether amphibole is a primary mineral formed during melt-rock interaction with the volcanic host, or if it formed as a result of post-magmatic alteration (cf. O'Connor et al., 1996). In some instances, amphibole is associated with small amounts of light yellow to reddish brown glass as linings of vugs around spinel, tentatively indicating that it formed during melt-rock interaction. Detailed thin section analysis did not reveal any phlogopite in the samples, although traces of Ti-rich phlogopite are present in some mantle xenoliths from the Meerfelder Maar (Witt-Eickschen et al., 1998).

The measured density of the starting material was 3.326 g/cm^3 and there was no detectable loss on ignition. While Mössbauer analysis revealed no detectable Fe(III), the magnetic susceptibility (SI) of the starting material was 12.86, suggesting that trace amounts of ferromagnetic minerals were present in the starting material.

The harzburgite xenolith was cored with a diamond drill bit and cut with a diamond saw blade into 6 pieces (each having a volume of ~1cm^3) to recover fresh

cohesive material. The pieces were then thoroughly rinsed in deionized water and stored in a drying oven at 40 °C until loaded into the hydrothermal apparatus.

In the experiment, we reacted the harzburgite with an aqueous fluid of seawater chlorinity devoid of Mg and SO_4 and enriched in Ca and K (Table 3). This fluid chemistry was designed to represent seawater that had evolved during low-temperate alteration of rocks and precipitation of secondary minerals in recharge zones of mid-ocean ridge environments (Mottl, 1983).

RESULTS

Fluid chemistry - During the course of the experiment, some aqueous species concentrations remained relatively constant while others were characterized by relatively large changes (Figure 3 and Table 3). The pH (25 °C) increased from 6.3 at the beginning of the experiment to 9.0 at its termination. The concentrations of dissolved Na, K, and Mg did not change significantly with time. In contrast, the concentration of dissolved Ca decreased from 30.5 to 27.6 mmol/kg during the experiment. After an initial increase in the concentration of Si from below detection in the starting fluid to 0.64 mmol/kg in the first sample at 122 h, its concentration decreased to 0.05 mmol/kg after 13441 hours of reaction.

The measured concentration of $H_{2(aq)}$ increased to 7.7 mmol/kg by the end of the experiment; however, the rate of $H_{2(aq)}$ concentration increase was not uniform throughout the experiment (Fig. 4), being fastest early during the experiment and then decreasing significantly over time.

Petrographic observations - Petrographic observations are summarized in Table 4. Thin section image analysis of the reacted harzburgite revealed that ~5 vol.% of the rock consists of secondary minerals formed during the experiment. The extent of serpentinization was greatest on the exterior rock surface and decreased toward the center of the rock. Reaction rims around primary minerals on the exterior rock surface are generally thicker than reaction rims located along internal fractures. Primary minerals are partly replaced or overgrown by secondary minerals. Primary silicates, including olivine and orthopyroxene, show abundant indications of dissolution such as lenticular etch pits, cone-shaped etch pits, en echelon (sawtooth) etch pits, and denticles (Figs. 5e, 5f, 6e, 6f). Some dissolution features reveal a preferred orientation and an almost equidistant periodicity (Fig. 6e). In numerous instances, intragranular fractures initiate at cone-shaped etch pits similar to those observed in partially serpentinized abyssal peridotite (Figs. 6f, 7f; cf. Klein et al., 2009; Plümper et al., 2012). Cr-spinel and clinopyroxene do not show any visible signs of dissolution (Figs. 6c, 7d, 7e).

Inspection of the reacted rock exterior revealed a reaction rim consisting of lizardite + chrysotile ± magnetite ± chlorite ± calcite (Figs. 5, 6). The mineralogy of the reaction rim varies systematically with its precursor mineral (Fig. 4a). Olivine is covered by a layer mainly consisting of lizardite intergrown with accessory magnetite (Fig. 5c, 6a). The latter is also found directly at the olivine surface. In contrast, lizardite forms a monomineralic layer covering orthopyroxene. In both instances, the lizardite layer is overgrown by chrysotile, which forms the outermost layer (Fig. 6a, b, g). Chrysotile is often intergrown with lizardite and minor chlorite

299 forming cactus-like protrusions (Fig. 5a, b). In most areas, the thickness of the
300 reaction rim around olivine and orthopyroxene varies between 50 and 70μm (Fig.
301 6a, b, c, g); however, some embayed areas measure up to 0.5 mm. While
302 clinopyroxene appears to be unaltered, it is in places overgrown by a thin (~5-
303 10μm) layer of polyhedral serpentine and magnetite filling void spaces overgrown
304 by chrysotile (Fig. 7d). Lizardite, chrysotile, and polyhedral serpentine form geode-
305 like compartments on the rock exterior and host sub- to euhedral magnetite (Figs.
306 5a, c). Chrysotile fibers are about 0.1 to 0.2 μm thick and are up to several tens of μm
307 long (Fig. 5b, 5a, g). Subhedral magnetite, ca. 1 μm to 40 μm in diameter (Figs. 5, 6),
308 and euhedral calcite crystals (ca. 5 μm to 200μm in diameter, Figs. 5d, 7c), are
309 embedded in the serpentine matrix. In contrast to magnetite, calcite is found
310 exclusively on the exterior rock surface. In a few instances, the walls of geode-
311 shaped features hosted by spinel, clinopyroxene, and accessory amphibole are
312 coated with euhedral chlorite (Fig. 5g). Chlorite in geodes likely formed at the
313 expense of amphibole as clinopyroxene and spinel (Fig. 7d, e) appear to be
314 unaltered.

315 Thin section examination of the rock interior reveals incipient replacement
316 textures after olivine (mesh texture, Fig. 6d) and orthopyroxene (bastite texture, Fig.
317 6g). Mesh texture is mainly composed of lizardite and minor magnetite, whereas
318 brucite is lacking. In numerous instances magnetite formed directly at the olivine
319 surface (cf. Beard et al., 2009; Frost et al., 2013) during incipient serpentinization
320 (Figs. 6a, 6b, 6e, 6f, 7e). Bastite texture features intergrowths of lizardite and

chlorite, but lacks magnetite and talc. Contacts between mesh and bastite texture are remarkably sharp (Fig. 6b).

The width of veins ranges from <1μm to ~100μm and decreases away from the rock surface toward the rock interior (e.g., Fig. 6e). High resolution confocal Raman spectroscopy revealed that veins cross-cutting olivine are composed of lizardite (Fig. 8) and accessory magnetite, but lack brucite (cf. Beard et al., 2009; Frost et al., 2013). Magnetite grains in veins are smaller and less abundant than on the rock exterior, anhedral and irregularly distributed. They precipitated directly at the olivine surface and within the serpentine vein matrix. Where an Al- and Si-rich glassy melt film was present between two adjacent olivine grains (cf. O'Connor et al., 1996), traces of chlorite formed together with lizardite in the vein center. Veins cross-cutting pyroxene are composed of lizardite and chlorite. Neither magnetite nor talc formed at the expense of orthopyroxene.

Primary sulfides consisting of pentlandite ± pyrrhotite are irregularly distributed within the rock. Where fluid accessed primary sulfide, heazlewoodite ± magnetite precipitated (Fig. 7b). Heazlewoodite is also found in veins and possibly formed from Ni and S released during dissolution of olivine (Fig. 5f). Pentlandite is found together with magnetite; however, it remains unclear whether pentlandite was in equilibrium with magnetite (Fig. 7a). No evidence was found that awaruite, a common Ni-Fe alloy found in partly altered serpentinite (Klein and Bach, 2009), formed during the experiment.

343 *Composition of secondary minerals* - Lizardite and chrysotile do not reveal
344 systematic compositional differences that are discernible by electron microprobe
345 analysis. Conversely, systematic compositional differences exist between serpentine
346 forming at the expense of olivine and orthopyroxene, and between serpentine from
347 the exterior rock surface and the interior (Fig. 9, Table 5). On the rock exterior,
348 serpentine (lizardite and chrysotile) after olivine is on average Fe-poor (Mg# 97),
349 while serpentine after orthopyroxene is on average richer in Fe (Mg# 95), Al, and Cr.
350 In contrast, serpentine from the rock interior has lower Mg#s after olivine (~95)
351 and after orthopyroxene (~92). Serpentine in bastite texture on the exterior rock
352 surface is depleted in Fe relative to its precursor and forms sharp boundaries with
353 serpentine after olivine (Fig. 6b). Chlorite has a Mg# of ~90-91 regardless of its
354 proximity to olivine, orthopyroxene, or the rock exterior. Electron microprobe
355 analysis of bastite texture in the rock interior revealed substantially higher Al
356 contents compared with bastite on the rock surface, which can be attributed to
357 variable contents of chlorite interwoven with serpentine. Magnetite shows
358 negligible compositional variations with scanning electron microscope energy
359 dispersive spectroscopy. Heazlewoodite is nearly of end-member composition with
360 minor impurities of Fe (2.2-3.9 wt.%) and Co (0.25-0.34 wt.%). Calcite is virtually
361 pure (Table 5) with only traces of MgO (0.04wt.%) and FeO (0.02 wt.%).
362
363 *Magnetite abundance* - The magnetic susceptibility increased from SI (x 10^{-5})= 12.86
364 to 72.23 and saturation magnetization increased from 3.4154e-7 Am^2 to 3.431e-5
365 Am^2, consistent with the precipitation of magnetite during the experiment. No other

366 ferromagnetic minerals were formed. Magnetization measurements suggest that the
367 bulk rock magnetite content was 0.19 wt.% after 13441 hours of reaction. Because
368 the bulk sample contained only ~5 vol.% of relatively Fe-poor serpentine and only a
369 fraction of the Fe in serpentine was ferric, the bulk Fe(III) was below the detection
370 limit of Mössbauer spectroscopy (~1% bulk Fe(III)).
371

372 **DISCUSSION**

373 *Serpentinization progress* - Serpentinization leads to a decrease in rock density as
374 higher density primary minerals are replaced with lower density secondary
375 minerals (except for magnetite, Ni-Fe sulfides and alloys). The extent of
376 serpentinization can be roughly approximated using the empirical relation $\rho = 3.30$
377 $- 0.785S$, with ρ being the rock density and S being the fraction of rock which has
378 been serpentinized (Miller and Christensen, 1997). During our experiment, the rock
379 density decreased from an initial value of 3.326 g/cm^3 to 3.258 g/cm^3, which based
380 on the empirical relation yields $S \approx 5\%$.

381 To get an independent estimate for the extent of alteration, we employed a
382 linear relationship between saturation magnetization (Js) and extent of
383 serpentinization (S): $Js = 8.979 \times 10^{-4} \times S$ (Malvoisin et al., 2012b). Using this
384 relationship, the increase in the measured magnetization saturation during the
385 experiment, $Js_{end} - Is_{initial} = 3.397 \times 10^{-5} Am^2$ suggests that 3.8 % of the protolith
386 underwent serpentinization.

387 Dissolution rates of primary silicates can be estimated by the release of
388 elements to solution as a function of time (Wogelius and Walther, 1991). In our

experiment, dissolved Mg, Fe, and Si released by dissolution of olivine and orthopyroxene were immediately consumed during precipitation of serpentine, magnetite, and chlorite, precluding their use for rate estimates. In contrast, H_2 released to solution, as Fe(II) in primary minerals was oxidized to Fe(III) in serpentine and magnetite, is not consumed during mineral precipitation. Therefore, $H_{2(aq)}$ release can be used as an indicator of alteration progress. The generalized reaction can be represented as:

(1) $2FeO + H_2O = Fe_2O_3 + H_{2(aq)}$

where FeO and Fe_2O_3 represent components of primary and secondary minerals, respectively. Since ferroan brucite did not form during the experiment, the protolith fraction that underwent serpentinization at the time of fluid sampling can be estimated. Given that the protolith has an FeO content of ~7.67 wt.% (with negligible Fe(III) content) (Table 1), and assuming that 2/3 of the Fe in completely serpentinized peridotite is Fe(III) (Andreani et al., 2013; Klein et al., 2014; Marcaillou et al., 2011), complete serpentinization of 18.19 g peridotite at the experimental conditions would release ~ 6.4 mmol $H_{2(aq)}$. After correcting for the amount of H_2-bearing fluid removed during each of the six sampling occasions (Table 3), the total amount of H_2 released after 13441 hours of reaction was 0.24 mmol, suggesting that ~3.8 mol % of the protolith underwent serpentinization. This value is consistent with the reaction extent estimated from magnetization saturation measurements. Factoring in a volume increase of 40% during

412 serpentinization (see below) these estimates are consistent with thin section
413 observations, but are slightly lower than density changes would suggest.
414 Most laboratory serpentinization experiments used powdered reactants,
415 making a straightforward comparison of reaction progress with our estimates
416 difficult. Malvoisin and Brunet (2014) reacted a sintered San Carlos olivine
417 aggregate with water at 300°C and 50MPa for 6956 hours. About 2.66 % of the
418 olivine underwent serpentinization, suggesting that, despite some apparent
419 differences in protolith composition, overall reaction rates were similar to those in
420 our experiment.
421
422 *Mass transfer* - Serpentinization involves many chemical components, but the basic
423 mechanisms can be understood by considering the following reactions in the system
424 MgO-SiO_2-H_2O (Bowen and Tuttle, 1949; Johannes, 1968; Kitahara et al., 1966):
425
426 (2) $2Mg_2SiO_4 + 3H_2O = Mg_3Si_2O_5(OH)_4 + Mg(OH)_2$
427 forsterite serpentine brucite
428
429 (3) $3Mg_2Si_2O_6 + 3H_2O = Mg_3Si_2O_5(OH)_4 + Mg_3Si_4O_{10}(OH)_2$
430 enstatite serpentine talc
431
432 (4) $2Mg_2SiO_4 + Mg_2Si_2O_6 + 4H_2O = 2Mg_3Si_2O_5(OH)_4$
433 forsterite enstatite serpentine
434

In a closed system, serpentinization of forsterite leads to the formation of serpentine and brucite (2), whereas serpentinization of enstatite leads to the formation of serpentine and talc (3). If forsterite and enstatite undergo simultaneous serpentinization at a 2:1 molar ratio, neither brucite nor talc is formed and the only reaction product is serpentine (4). Indeed, our experiment produced mainly serpentine without any talc (Fig. 6g) or brucite (Fig. 8) suggesting that alteration of olivine and orthopyroxene proceeded according to reaction 4. Since reaction 4 is a composite of reactions:

(5) $3Mg_2SiO_4 + 4H_2O + SiO_{2(aq)} = 2Mg_3Si_2O_5(OH)_4$

forsterite serpentine

(6) $3Mg_2Si_2O_6 + 4H_2O = 2Mg_3Si_2O_5(OH)_4 + 2SiO_{2(aq)}$

enstatite serpentine

(7) $2Mg_2SiO_4 + H_2O + 2H^+ \rightarrow Mg_3Si_2O_5(OH)_4 + Mg^{2+}$

forsterite serpentine

(8) $Mg_2Si_2O_6 + Mg^{2+}\ 3H_2O \rightarrow Mg_3Si_2O_5(OH)_4 + 2H^+$

enstatite serpentine

it appears that the formation of serpentine involves mass transfers of $SiO_{2(aq)}$, Mg^{2+}, and H^+ between the olivine and orthopyroxene reaction fronts. To evaluate mass

transfer during the experiment, we calculated the *in situ* speciation of analyzed fluid compositions using the software code EQ3/6 (Wolery, 1992) and plotted the computed values in an activity-activity diagram (Fig. 10). This diagram was constructed using equilibrium constants calculated with the software code SUPCRT92 (Johnson et al., 1992) and assuming a water activity of 1. Detailed information about thermodynamic data, activity models, etc. used in the calculations has been published elsewhere (Klein et al., 2009; 2013; McCollom and Bach, 2009).

The main driving force for $SiO_{2(aq)}$ mass transfer is a steep activity (a) gradient between reactions 5 (equilibrium log $a SiO_{2(aq)}$ = -5.681) and 6 (equilibrium log $a SiO_{2(aq)}$ = -0.873) at the experimental conditions. Speciation calculations of *in situ* fluid compositions reveal log $a SiO_{2(aq)}$ values ranging from -3.2 to -4.3, which plot between reactions 5 and 6 (Fig. 10), consistent with $SiO_{2(aq)}$ released by reaction 6 being consumed by reaction 5. As for the steep gradient in $a SiO_{2(aq)}$ between reactions 5 and 6, there are steep gradients in the activities of Mg^{2+} and H^+ (pH) between reactions 7 and 8. At the experimental conditions, equilibrium values of log($a Mg^{2+}/a^2H^+$) for reactions 7 and 8 are 7.96 and 4.75, respectively, assuming pure Mg-endmember minerals and a water activity of 1. The calculated *in situ* pH values ranged between 5.2 and 6.2. Speciation calculations of *in situ* fluid composition reveal log ($a Mg^{2+}/a^2H^+$) values between 5.0 and 6.9, consistent with Mg^{2+} released by reaction 7 being consumed by reaction 8, and with H^+ released by reaction 8 being consumed by reaction 7. Thus, it appears that mass transfer was coupled and proceeded in both directions between olivine and orthopyroxene reaction fronts.

Clinopyroxene does not show any obvious signs of dissolution (Figs. 6c, 7d) suggesting that it did not have a significant impact on mass transfer during the onset of serpentinization at the experimental conditions.

Formation of serpentine according to reaction 4 requires the reaction of 2 moles of forsterite for each mole of enstatite reacted. Because the starting material had ~4 times more olivine than orthopyroxene on a molar basis, and given that Mg and Si released during dissolution of both minerals were immediately consumed by serpentine precipitation, orthopyroxene must have reacted significantly faster than olivine to fulfill the mass balance. However, since olivine/orthopyroxene mass ratios vary on a mm to cm scale, it remains difficult to further constrain individual reaction rates from our experiment.

Reaction pathways during serpentinization - Thermodynamic phase relations suggest that complete serpentinization of peridotite leads to the formation of serpentine + brucite ± magnetite (in addition to a number of accessory minerals) (Klein et al., 2009; Klein et al., 2013; McCollom and Bach, 2009), and that this would have been the final mineral assemblage had the experiment gone to completion. However, the experimental results show that incipient serpentinization at the experimental conditions did not involve the formation of brucite, indicating that serpentinization must be regarded as a sequence of individual reactions that define a reaction path (cf. Bach et al., 2004; 2006).

As discussed in the previous section, mass balance constraints require that orthopyroxene dissolution is significantly faster than dissolution of olivine at

504 temperatures of ~300°C. Because orthopyroxene is less abundant than olivine in
505 peridotite, orthopyroxene will be exhausted from the equilibrium mineral
506 assemblage first. Once orthopyroxene approaches exhaustion, dissolution of olivine
507 will dominate and result in the formation of serpentine and brucite (plus magnetite)
508 as depicted in reaction 2 until olivine is exhausted. The final assemblage of
509 secondary minerals will therefore include serpentine, brucite, and magnetite (in
510 addition to traces of other minerals).

511 This reaction path is only valid for temperatures close to 300°C and
512 peridotite protolith compositions. Serpentinization can take place at temperatures
513 >350°C, as evidenced by direct temperature measurements of fluids emanating from
514 the ultramafic-influenced Logatchev, Nibelungen and Rainbow hydrothermal fields
515 (Douville et al., 2002; Schmidt et al., 2011; Schmidt et al., 2007). Allen and Seyfried
516 (2003) reacted powdered lherzolite with a NaCl-$MgCl_2$ bearing fluid at 400°C and 50
517 MPa for 1462 hours and found that orthopyroxene and clinopyroxene were coated
518 with alteration products, but olivine surfaces appeared unaltered. Indeed, while it is
519 predicted that olivine is part of the equilibrium mineral assemblage in the presence
520 of water at ~400°C (e.g., Klein et al., 2013), orthopyroxene and clinopyroxene are
521 unstable at these conditions. The reaction pathway of serpentinization at 400°C is
522 therefore very different from that at 300°C and will be dominated by the
523 precipitation of serpentine, talc, tremolite and chlorite at the expense of pyroxene.
524 Once pyroxene is exhausted from the equilibrium mineral assemblage,
525 serpentinization ceases unless the temperature decreases and olivine becomes
526 unstable in the presence of water.

Lower temperatures of serpentinization of 250°C or less are expected in areas where magma-supply and thus heat is limited, such as in off-axis hydrothermal systems like Lost City (Foustoukos et al., 2008; Kelley et al., 2001), forearc settings of subduction zones (Fryer, 2012), and along magma-poor continental rifted margins (e.g., Klein et al., 2014). At these temperatures, the presence of relict orthopyroxene and brucite in the alteration mineral assemblage may indicate that olivine dissolution was faster than orthopyroxene dissolution (cf. Martin and Fyfe, 1970). If this is true, then olivine may be consumed during serpentinization before orthopyroxene. Once olivine approaches exhaustion from the primary mineral assemblage, the dissolution of remaining orthopyroxene will dominate the reaction path. Its dissolution provides excess silica, which is available to react with some of the brucite to form additional serpentine and possibly magnetite (Bach et al., 2006; Beard et al., 2009). Although the final secondary mineral assemblage would be the same as that for serpentinization at 300°C, the pathway is markedly different. It is important to note that magnetite formation is limited during serpentinization of peridotite at temperatures lower than ~200°C, because Fe is preferentially taken up by brucite (Klein et al., 2013; 2014; Seyfried et al., 2007).

Serpentinization in different rock domains –The exterior rock surface and the rock interior reveal mineralogical, chemical, and textural differences. For example, secondary minerals on the rock exterior show well-developed crystal habits, whereas those within the rock do not. Euhedral calcite is present on the rock

exterior but did not precipitate in the rock interior. It precipitated from the bulk solution surrounding the rock, which was apparently saturated with calcite, in contrast to fluid in the rock interior. It is noteworthy that calcite precipitated at all, since conditions in the surrounding fluid were relatively reducing. However, it remains unclear what condition hindered calcite from precipitating within the rock. Differences in the compositions of serpentine from the rock exterior and interior (Fig. 9) may reflect distinct fluid-to-rock mass ratios (F/R) and differences in fluid chemistry. Klein et al. (2009) predicted changes in fluid chemistry, mineralogy, and mineral chemistry as a function of F/R for serpentinization of harzburgite. Serpentine is predicted to become richer in Fe with decreasing F/R. Indeed, field studies suggest that lizardite in veins formed during rock-dominated serpentinization is Fe-rich relative to chrysotile in veins formed under open system conditions (Beard et al., 2009; Frost et al., 2013). Chrysotile in the rock exterior may have formed under similar conditions, with slowly moving or stagnant pore fluids in fractures. In contrast, serpentinization of the rock interior possibly occurred at conditions similar to those in rock-dominated domains, away from larger fractures in hydrothermal systems.

Hydrogen release, volume changes, and reaction driven fracturing - The concentrations of H_2 released during serpentinization have been measured in several previous laboratory experiments (Allen and Seyfried, 2003; Berndt et al., 1996; Jones et al., 2010; Klein and McCollom, 2013; Mayhew et al., 2013; McCollom and Seewald, 2001; Neubeck et al., 2011; Seyfried et al., 2007). Comparison of the

573 results presented here with previous studies at 200 and 400°C conducted in flexible
574 gold bag reaction vessels show similar temporal trends (Fig. 4). It is important to
575 note, however, that the absolute values of measured H_2 concentrations are not
576 directly comparable due to differences in starting materials, grain sizes, fluid-to-
577 rock mass ratios (F/R), and temperatures. In most experiments, H_2 concentrations
578 increase with time and extent of serpentinization. There is no clear distinction
579 between experiments using powdered olivine and peridotite as initial reactants. A
580 comparison of the H_2 concentrations measured by Berndt et al (1996) and Klein and
581 McCollom (2013) suggests that the release rate of H_2 is strongly influenced by grain
582 size (surface area) of the starting materials (cf. Malvoisin et al., 2012b). A common
583 feature of some experiments is that aqueous H_2 concentrations increase rapidly
584 shortly after the beginning of an experiment, as primary mineral surfaces are
585 directly exposed to the interacting fluid. The rate of increase in H_2 concentration
586 decreases significantly with time. This behavior is most pronounced in our
587 experiment. The decreased rate of H_2 production cannot be explained with
588 exhaustion of reactants, because primary silicates were present until the
589 experiment was terminated. Moreover, olivine and orthopyroxene remained far
590 from equilibrium throughout the experiment (Fig. 10). Therefore, other mechanisms
591 must have caused the decreased H_2 release rate. Thin section petrography revealed
592 filling of fractures and coating of primary mineral surfaces suggesting reduced fluid
593 access to primary minerals with time and reduced rates of serpentinization and H_2
594 generation. Godard et al. (2013) reached similar conclusions based on flow-through
595 serpentinization experiments that involved sintered olivine as the starting material.

In our experiment, serpentinization reactions consumed water but did not release significant amounts of dissolved species other than H_2. Thus hydration reactions must have led to a substantial volume increase. Again, because neither brucite nor talc formed during the experiment, it follows that incipient serpentinization was dominated by reaction 4 during our experiment. The volume increase for this reaction is ca. 40%, which accounts for the observed fracture filling.

The self-sealing behavior of serpentinization is at odds with field observations of high degrees of serpentinization of abyssal peridotites. However, MacDonald and Fyfe (1985) proposed that volume expansion leads to buildup of stress and episodic cracking that creates permeability and provides water access to fresh mineral surfaces. Thin section petrography suggests that grain boundaries and cracks already present in the protolith (Figs. 1, 2) were preferentially exploited by serpentinization reactions (cf. Rouméjon and Cannat, 2014). The stress increase due to volume expansion was sufficient to induce further cracking during our experiment, in particular along cone-shaped etch pits (e.g., Figs. 6f, 7f). These etch pits and associated fractures were not observed in the starting material (Fig. 2), suggesting the creation of new fluid flow paths during the experiment.

IMPLICATIONS

The results of our laboratory experiment provide new insights into geochemical processes during incipient serpentinization of peridotite at conditions representative of hydrothermal subseafloor reaction zones. Our experimental results imply that orthopyroxene reacts significantly faster than olivine at

temperatures of ~300°C, which precludes brucite formation early during serpentinization. This result implies that serpentinization of peridotite at similar conditions proceeds in two consecutive steps. First, serpentine and minor amounts of magnetite and chlorite form at the expense of olivine and orthopyroxene. Second, once the less abundant orthopyroxene approaches exhaustion, dissolution of olivine will produce serpentine, brucite and magnetite. While this is the same alteration assemblage produced by serpentinization at lower temperatures, the reaction pathways are different due to variations in thermodynamic phase relations and dissolution kinetics of primary minerals.

Serpentine precipitation during incipient alteration of peridotite appears to be mediated by coupled mass transfer of $SiO_{2(aq)}$, Mg^{2+}, and H^{+} along steep activity gradients between the olivine and orthopyroxene reaction fronts. Dissolved Si and Mg released during dissolution of olivine and orthopyroxene were consumed by precipitating serpentine, further supporting the idea that serpentinization can involve a significant increase in volume and a decrease in permeability.

Our experimental results imply that the release rate of H_2 is limited by water access to primary mineral surfaces and that serpentinization is, to some extent, a self-sealing process. However, many abyssal peridotites are strongly fractured and completely altered suggesting that fracturing promotes water ingress and allows serpentinization to progress rapidly relative to geological timescales. Fracturing may therefore have far-reaching implications for the rate of H_2 production in subseafloor serpentinization systems.

Acknowledgements

This study was partially supported by the National Science Foundation (NSF-OCE grants 1059534 to F.K. and S.E.H and OCE-0927744 to T.M.M.) and the Deep Ocean Exploration Institute at the Woods Hole Oceanographic Institution. We thank Sean Sylva, Margaret Sulanowska, and Jim Eckert for their outstanding support with sample analysis and Horst Marschall for letting us use his petrographic microscope and SEM. We also thank Nick Pester, Anna Neubeck, and Associate Editor Dionysis Foustoukos for helpful and constructive reviews that greatly improved the manuscript. The IRM is supported by the Instruments and Facilities Program of the NSF Division of Earth Science. This is IRM contribution 1410.

Figure captions

Figure 1. Thin section photomicrograph mosaics of harzburgite used as the starting material in the experiment in cross-polarized light (left) and plane polarized light (right). Ol = olivine, Opx = orthopyroxene, Cpx = clinopyroxene, Hbl = hornblende, Spl = spinel.

Figure 2. Back scattered electron images of the fractured, unaltered protolith. Mineral abbreviations are the same as in Fig. 1.

664 **Figure 3.** Changes in fluid chemistry measured during the experiment. Note the
665 concentration 'breaks' in the ordinate.
666
667 **Figure 4.** Measured $H_{2(aq)}$ concentrations as a function of time. Hydrogen
668 concentrations measured during previous experiments are shown for comparison.
669 F/R = initial fluid to rock mass ratio. See text for discussion.
670
671 **Figure 5.** Back scattered electron images of minerals on exterior surfaces of the
672 rock after 13441 hours of reaction. (a, b, c) Chrysotile (Ctl), lizardite (Lz), polyhedral
673 serpentine (P-Srp), and magnetite on relict olivine. Details of (a) are illustrated in
674 (b) and (c). (d) Euhedral calcite (Cal) and Ctl. (e) Relict orthopyroxene (Opx)
675 showing abundant dissolution features. (f) Sawtooth vein composed of Lz, magnetite
676 (Mag), and heazlewoodite (Hzl) cross-cutting relict olivine (Ol). (g) Chlorite (Chl)
677 geode surrounded by relict clinopyroxene (Cpx), Cr-spinel (Spl), and Ol. (h)
678 Overview image showing areas depicted in (a, solid white line) and (g, dashed white
679 line).
680
681 **Figure 6.** Back scattered electron images of thin sections through the rock after
682 13441 hours of reaction. (a) Overview image of images b (white dashed line) and c
683 (black dashed line) showing relict Opx and Ol and a typical ~70 μm thick reaction
684 rim at the rock surface composed of Lz + Ctl ± Mag. (b) Lz surrounding Opx (light
685 gray) is significantly richer in Fe than Lz surrounding Ol (dark gray). Fe-rich and Fe-
686 poor Lz form sharp fronts and are in clear disequilibrium. Note that Mag is found

687 directly at the Ol surface (cf. Beard et al., 2009) and within the reaction rim. (c) Cpx
688 exsolution lamellae (white) in Opx apparently unaffected by serpentinization. (d)
689 Incipient formation of pseudomorphic mesh texture along former olivine (sub-)
690 grain boundaries. (e) Sawtooth vein composed of Lz and minor Mag cross-cutting
691 relict Ol. (f) Vein composed of Lz and Mag cross-cutting relict Ol. Note the cone-
692 shaped dissolution features in Ol and extending cracks (white arrow). (g) Mag-free
693 bastite pseudomorph after Opx. Mineral abbreviations are the same as in Fig. 5.
694
695 **Figure 7.** Back scattered electron images of minor phases (a-c), apparently
696 unreactive phases (d-e), and an intra-olivine fracture extending from a cone-shaped
697 etch pit (f). (a) Opaque phase assemblage composed of pentlandite (Pn) and Mag.
698 (b) Opaque phase assemblage composed of Hzl and Mag. (c) Large subhedral grain
699 of Cal. (d) Typical Cpx at rock surface with well defined subhedral crystal faces. This
700 may suggest that Cpx alteration was insignificant. Polyhedral serpentine (P-Srp)
701 appears to be associated with Cpx, but it remains unclear whether P-Srp formed at
702 its expense. (e) Unaltered Spl surrounded by partially serpentinized Ol in mesh
703 texture. (f) Magnified image of cone-shaped etch pit and fracture shown in (e, white
704 dashed box).
705
706 **Figure 8**. False color Raman map of representative Lz vein (green) cross-cutting
707 relict Ol (red) within the rock interior. These veins do not host any brucite. Note that
708 we avoided areas with abundant magnetite for the map. Detailed Raman analysis

reveal that, where present, magnetite is not associated with brucite. The spatial resolution is ~1μm.

Figure 9. Electron microprobe analysis of serpentine after olivine and serpentine-chlorite intergrowths after orthopyroxne in different rock textures and domains. The terms 'bastite' and 'mesh' refer to pseudomorphic replacement textures after orthopyroxene and olivine, respectively.

Figure 10. Activity-activity diagram for the system CaO-MgO-SiO_2-H_2O at 300°C and 35 MPa calculated with the software code SUPCRT92 (Johnson et al., 1992) assuming $a H_2O = 1$. The speciated activities of measured fluid compositions fall in the chrysotile field (representative of serpentine). Sample numbers refer to those listed in Table 3. The dashed red lines depict the $SiO_{2(aq)}$ activities for metastable equilibrium according to reactions 5 and 6. The blue line denotes the solubility of quartz. Note that monticellite does not occur in serpentinite. Its formation is therefore suppressed.

References

Allen, D. E., and Seyfried, W. E. J. (2003) Compositional controls on vent fluids from ultramafic-hosted hydrothermal systems at mid-ocean ridges: An experimental study at 400ºC, 500 bars. Geochimica et Cosmochimica Acta, 67, 1531-1542.

Alt, J. C., Schwarzenbach, E. M., Früh-Green, G. L., Shanks Iii, W. C., Bernasconi, S. M., Garrido, C. J., Crispini, L., Gaggero, L., Padron-Navarta, J. A., and Marchesi, C. (2013) The role of serpentinites in cycling of carbon and sulfur. Seafloor serpentinization and subduction metamorphism. Lithos, 178, 40-54.

Alt, J. C., and Shanks, W. C., (1998) Sulfur in serpentinized oceanic peridotites: Serpentinization processes and microbial sulfate reduction. Journal of Geophysical Research, 103, 9917-9929.

Alt, J. C., and Shanks, W. C. (2003) Serpentinization of abyssal peridotites from the MARK area, Mid-Atlantic Ridge. Sulfur geochemistry and reaction modeling: Geochimica Cosmochimica Acta, 67, 641-653.

Andreani, M., Munoz, M., Marcaillou, C., and Delacour, A. (2013) µXANES study of iron redox state in serpentine during oceanic serpentinization. Lithos, 178, 70-83.

Armstrong, J. T. (1995) CITZAF: A package of correction programs for the quantitative electron microbeam X-ray analysis of thick polished materials, thin films, and particles. Microbeam Analysis, 4, 177-200.

Bach, W., Garrido, C. J., Harvey, J., Paulick, H., and Rosner, M. (2004) Seawater-peridotite interactions – First insights from ODP Leg 209, MAR 15ºN.

Geochemistry, Geophysics, Geosystems 5, Q09F26, doi: 10.1029/2004GC000744.

Bach, W., Paulick, H., Garrido, C. J., Ildefonse, B., Meurer, W. P., and Humphris, S. E. (2006) Unraveling the sequence of serpentinitzation reactions: petrography, mineral chemistry, and petrophyscis of serpentinites from MAR 15ºN (ODP Leg 209, Site 1274). Geophysical Research Letters 33, L13306, doi:10.1029/2006GL025681.

Bach, W., Jöns, N., and Klein, F. (2013) Metasomatism within the ocean crust. *in* Metasomatism and the Chemical Transformation of Rock, Halrov, D., and Austrheum, H., eds., Springer Berlin Heidelberg, 253-288.

Beard, J. S., Frost, B. R., Fryer, P., McCaig, A., Searle, R., Ildefonse, B., Zinin, P., and Sharma, S. K. (2009) Onset and progression of serpentinization and magnetite formation in olivine-rich troctolite from IODP Hole U1309D. J. Petrology, 50, 387-403.

Berndt, M. E., Allen, D. E., and Seyfried, W. E. (1996) Reduction of CO_2 during serpentinization of olivine at 300°C and 500 bars. Geology, 24, 351-354.

Bodinier, J. L., and Godard, M. (2007) Orogenic, ophiolitic, and abyssal peridotites. Treatise on Geochemistry: Oxford, Pergamon, 1-73.

Bowen, N. L., and Tuttle, O. F. (1949) The system MgO-SiO_2-H_2O. Geological Society of America Bulletin, 60, 439-460.

Brazelton, W. J., Nelson, B., and Schrenk, M. O. (2012) Metagenomic evidence for H_2 oxidation and H_2 production by serpentinite-hosted subsurface microbial communities. Frontiers in Microbiology, doi: 10.3389/fmicb.2011.00268.

770 Chamberlain, J. A., McLeod, C. R., Traill, R. J., and Lachance, G. R. (1965) Native
771 metals in the Muskox intrusion. Canadian Journal of Earth Sciences, 2, 188-215.
772 Coleman, R. G. (1971) Petrologic and geophysical nature of serpentinites. Geol. Soc.
773 Am. Bull., 82, 897-918.
774 Craddock, P. R., Warren, J. M., and Dauphas, N. (2013) Abyssal peridotites reveal the
775 near-chondritic Fe isotopic composition of the Earth. Earth and Planetary Science
776 Letters, 365, p. 63-76.
777 Deschamps, F., Guillot, S., Godard, M., Andreani, M., and Hattori, K. (2011)
778 Serpentinites act as sponges for fluid-mobile elements in abyssal and subduction
779 zone environments. Terra Nova, 23, 171-178.
780 Dick, H. J. B. (1989) Abyssal peridotites, very slow spreading ridges and ocean ridge
781 magmatism, *in* Saunders, A. D., and Norry, M. J., eds., Magmatism in the Ocean
782 Basins: Oxford, Blackwell, 71-105.
783 Douville, E., Charlou, J. L., Oelkers, E. H., Bianvenu, P., Jove Colon, C. F., Donval, J.
784 P., Fouquet, Y., Prieur, D., and Appriou, P. (2002) The Rainbow vent fluids
785 (36°14'N, MAR): the influence of ultramafic rocks and phase separation on trace
786 metal contents on Mid-Atlantic Ridge hydrothermal fluids. Chemical Geology,
787 184, 37-48.
788 Escartin, J., Hirth, G., and Evans, B. (2001) Strength of slightly serpentinized peridotites:
789 Implications for the tectonics of oceanic lithosphere. Geology, 29, 1023-1026.
790 Escartín, J., Hirth, G., and Evans, B. (1997) Effects of serpentinization on the lithospheric
791 strength and the style of normal faulting at slow-spreading ridges: Earth and
792 Planetery Science Letters, 151, 181-189.

793 Foustoukos, D. I., Savov, I. P., and Janecky, D. R. (2008) Chemical and isotopic
794 constraints on water/rock interactions at the Lost City hydrothermal field, 30°N
795 Mid-Atlantic Ridge. Geochimica et Cosmochimica Acta, 72, 5457-5474.
796 Foustoukos, D. I., and Seyfried, W. E. (2004) Hydrocarbons in hydrothermal vent fluids.
797 the role of chromium-bearing catalysts: Science, 304, 1002-1005.
798 Frost, B. R., Evans, K. A., Swapp, S. M., Beard, J. S., and Mothersole, F. E., (2013) The
799 process of serpentinization in dunite from New Caledonia. *Lithos,* 24-39.
800 Früh-Green, G. L., Kelley, D. S., Bernasconi, S. M., Karson, J. A., Ludwig, K. A.,
801 Butterfiled, D. A., Boschi, C., and Proskurowski, G. (2003) 30,000 years of
802 hydrothermal activity at the Lost City vent field. Science, 301, 495-498.
803 Fryer, P. (2012) Serpentinite Mud Volcanism. Observations, Processes, and Implications.
804 Annual Review of Marine Science 4, 345-373.
805 Godard, M., Luquot, L., Andreani, M., and Gouze, P. (2013) Incipient hydration of
806 mantle lithosphere at ridges. A reactive-percolation experiment: Earth and
807 Planetary Science Letters, 371, 92-102.
808 Horita, J., and Berndt, M. E. (1999) Abiogenic methane formation and isotopic
809 fractionation under hydrothermal conditions. Science, 285, 1055-1057.
810 Hostetler, P. B., Coleman, R. G., Mumpton, F. A., and Evans, B. W. (1966) Brucite in
811 alpine serpentinites. American Mineralogist, 51, 75-98.
812 Iyer, K., Jamtveit, B., Mathiesen, J., Malthe-Sørenssen, A., and Feder, J. (2008)
813 Reaction-assisted hierarchical fracturing during serpentinization. Earth and
814 Planetary Science Letters, 267, 503-516.

Johannes, W. (1968) Experimental investigation of the reaction forsterite + H_2O = serpentine + brucite. Contributions to Mineralogy and Petrology, 19, 305-319.

Johnson, J. W., Oelkers, E. H., and Helgeson, H. C. (1992) SUPCRT92: A software package for calculating the standard molal thermodynamic properties of minerals, gases, aqueous species, and reactions from 1-5000 bars and 0-1000°C. Computers & Geosciences, 18, 899-947.

Jones, L. C., Rosenbauer, R., Goldsmith, J. I., and Oze, C. (2010) Carbonate control of H_2 and CH_4 production in serpentinization systems at elevated P-Ts. Geophysical Research Letters, 37, L14306.

Jöns, N., Bach, W., and Klein, F. (2010) Magmatic influence on reaction paths and element transport during serpentinization. Chemical Geology, 274, 196-211.

Kelemen, P. B., and Hirth, G., (2012) Reaction-driven cracking during retrograde metamorphism: Olivine hydration and carbonation. Earth and Planetary Science Letters, 345, 81-89.

Kelley, D. S., Karson, J. A., Blackman, D. K., Früh-Green, G. L., Butterfield, D. A., Lilley, M. D., Olson, E. J., Schrenk, M. O., Roe, K. K., Lebon, G. T., Rivizzigno, P., and Party, A.-S. (2001) An off-axis hydrothermal vent field near the Mid-Atlantic Ridge at 30°N. Nature, 412, 127-128.

Kitahara, S., Takenouchi, S., and Kennedy, G. C. (1966) Phase relations in the system MgO-SiO_2 -H_2O at high temperatures and pressures. American Journal of Science, 264, 223-233.

Klein, F., and Bach, W. (2009) Fe-Ni-Co-O-S phase relations in peridotite seawater interactions. Journal of Petrology, 50, 37-59.

838 Klein, F., Bach, W., Humphris, S. E., Kahl, W.-A., Jöns, N., Moskowitz, B., and Berquó,
839 T. S. (2014) Magnetite in seafloor serpentinite - Some like it hot. Geology, 42,
840 135-138.
841 Klein, F., Bach, W., Jöns, N., McCollom, T., Moskowitz, B., and Berquó, T. (2009) Iron
842 partitioning and hydrogen generation during serpentinization of abyssal
843 peridotites from 15°N on the Mid-Atlantic Ridge. Geochimica et Cosmochimica
844 Acta, 73, 6868-6893.
845 Klein, F., Bach, W., and McCollom, T. M. (2013) Compositional controls on hydrogen
846 generation during serpentinization of ultramafic rocks. Lithos, 178, 55-69.
847 Klein, F., and McCollom, T. M. (2013) From serpentinization to carbonation: New
848 insights from a CO_2 injection experiment. Earth and Planetary Science Letters,
849 379, 137-145.
850 Klügel, A., and Klein, F. (2006) Complex magma storage and ascent at embryonic
851 submarine volcanoes from the Madeira Archipelago. Geology, 34, 337-340.
852 Kodolanyi, J., Pettke, T., Spandler, C., Kamber, B. S., and Gmeling, K. (2012)
853 Geochemistry of ocean floor and fore-arc serpentinites: constraints on the
854 ultramafic input to subduction zones. Journal of Petrology, 53, 235-270.
855 Lang, S. Q., Butterfield, D. A., Schulte, M., Kelley, D. S., and Lilley, M. D. (2010)
856 Elevated concentrations of formate, acetate and dissolved organic carbon found at
857 the Lost City hydrothermal field. Geochimica et Cosmochimica Acta, 74, 941-
858 952.
859 Lister, C. R. B. (1974) On the penetration of water into hot rock. Geophysical Journal of
860 the Royal Astronomical Society, 39, 465-509.

Ludwig, K. A., Kelley, D. S., Butterfield, D. A., Nelson, B. K., and Früh-Green, G. (2006) Formation and evolution of carbonate chimneys at the Lost City Hydrothermal Field. Geochimica et Cosmochimica Acta, 70, 3625-3645.

Macdonald, A. H., and Fyfe, W. S. (1985) Rate of serpentinization in seafloor environments. Tectonophysics, 116, 123-135.

Maffione, M., Morris, A., Plümper, O., and van Hinsbergen, D. J. J. (2014) Magnetic properties of variably serpentinized peridotites and their implication for the evolution of oceanic core complexes. Geochemistry, Geophysics, Geosystems, 15, 923-944.

Malvoisin, B. and Brunet, F (2014). Water diffusion-transport in a synthetic dunite: Consequences for oceanic peridotite serpentinization. Earth and Planetary Science Letters 403, 263-272, 10.1016/j.epsl.2014.07.004.

Malvoisin, B., Brunet, F., Carlut, J., Rouméjon, S., and Cannat, M. (2012a) Serpentinization of oceanic peridotites: 2. Kinetics and processes of San Carlos olivine hydrothermal alteration. Journal of Geophysical Research, 117, B04102.

Malvoisin, B., Carlut, J., and Brunet, F. (2012b) Serpentinization of oceanic peridotites: 1. A high-sensitivity method to monitor magnetite production in hydrothermal experiments. Journal of Geophysical Research, 117, B01104.

Martin, B., and Fyfe, W. S. (1970) Some experimental and theoretical observations on the kinetics of hydration reactions with particular reference to serpentinization. Chemical Geology, 6, 185-202.

Mayhew, L. E., Ellison, E. T., McCollom, T. M., Trainor, T. P., and Templeton, A. S. (2013) Hydrogen generation from low-temperature water-rock reactions. Nature, 6, 478-484.

McCollom, T. M., and Bach, W. (2009) Thermodynamic constraints on hydrogen generation during serpentinization of ultramafic rocks. Geochimica et Cosmochimica Acta, 73, 856-875.

McCollom, T. M., and Seewald, J. S. (2001) A reassessment of the potential for reduction of dissolved CO_2 to hydrocarbons during serpentinization of olivine. Geochimica et Cosmochimica Acta, 65, 3769-3778.

Miller, D. J., and Christensen, N. I. (1997) Seismic velocities of lower crustal and upper mantle rocks from the slow-spreading Mid-Atlantic Ridge, south of the Kane transform zone (MARK). Proceedings of the Ocean Drilling Program Scientific Results, 153, 437-454.

Mottl, M. J. (1983) Metabasalts, axial hot springs, and the structure of hydrothermal systems at mid-ocean ridges. Geological Society of America Bulletin, 94, 161-180.

Nakamura, K., Morishita, T., Bach, W., Klein, F., Hara, K., Okino, K., Takai, K., and Kumagai, H. (2009) Serpentinized troctolites exposed near the Kairei Hydrothermal Field, Central Indian Ridge: Insights into the origin of the Kairei hydrothermal fluid supporting a unique microbial ecosystem. Earth and Planetary Science Letters, 280, 128-136.

903 Neubeck, A., Duc, N., Bastviken, D., Crill, P., and Holm, N. (2011) Formation of H_2 and
904 CH_4 by weathering of olivine at temperatures between 30 and 70°C. Geochemical
905 Transactions, 12, 6.
906 O'Connor, T. K., Edgar, A. D., and Lloyd, F. E. (1996) Origin of glass in Quaternary
907 mantle xenoliths from Meerfeldermaar, West Eifel, Germany: implications for
908 enrichment in the lithospheric mantle. Canadian Mineralogist, 34, 187-200.
909 O'Hanley, D. S. (1992) Solution to the volume problem in serpentinization. Geology, 20,
910 705-708.
911 Oufi, O., Cannat, M., and Horen, H. (2002) Magnetic properties of variably serpentinized
912 abyssal peridotite. Journal of Geophysical Research, 107,
913 10.1029/2001JB000549.
914 Page, N. J. (1967) Serpentinization at Burro Mountain, California. Contributions to
915 Mineralogy and Petrology, 14, 321-342.
916 Paulick, H., Bach, W., Godard, M., de Hoog, J. C. M., Suhr, G., and Harvey, J. (2006)
917 Geochemistry of abyssal peridotites (Mid-Atlantic Ridge, 15°20'N, ODP Leg
918 209): implications for fluid-rock interaction in slow spreading environments.
919 Chemical Geology, 234, 179-210.
920 Perner, M., Kuever, J., Seifert, R., Pape, T., Koschinsky, A., Schmidt, K., Strauss, H.,
921 and Imhoff, J. F. (2007) The influence of ultramafic rocks on microbial
922 communities at the Logatchev hydrothermal field, located 15°N on the Mid-
923 Atlantic Ridge. FEMS Microbiology Ecology, 61, 97-109.
924 Pester, N. J., Reeves, E. P., Rough, M. E., Ding, K., Seewald, J. S., and Seyfried Jr, W. E.
925 (2012) Subseafloor phase equilibria in high-temperature hydrothermal fluids of

926 the Lucky Strike Seamount (Mid-Atlantic Ridge, 37°N). Geochimica et
927 Cosmochimica Acta, 90, 303-322.
928 Plümper, O., Røyne, A., Magrasó, A., and Jamtveit, B. (2012) The interface-scale
929 mechanism of reaction-induced fracturing during serpentinization. Geology,
930 10.1130/G33390.1.
931 Proskurowski, G., Lilley, M. D., Kelley, D. S., and Olson, E. J. (2006) Low temperature
932 volatile production at the Lost City hydrothermal field, evidence from a hydrogen
933 stable isotope geothermometer. Chemical Geology, 229, 331-343.
934 Reynard, B., Mibe, K., and de Moortelèle, B. V. (2011) Electrical conductivity of the
935 serpentinised mantle and fluid flow in subduction zones. Earth and Planetary
936 Science Letters, 307, 387-394.
937 Rouméjon, S. and Cannat, M. (2014) Serpentinization of mantle-derived peridotites
938 at mid-ocean ridges: Mesh texture development in the context of tectonic
939 exhumation. *Geochemistry, Geophysics, Geosystems* 15, 2354-2379,
940 10.1002/2013gc005148.
941 Schmidt, K., Garbe-Schönberg, D., Koschinsky, A., Strauss, H., Jost, C. L., Klevenz, V.,
942 and Königer, P. (2011) Fluid elemental and stable isotope composition of the
943 Nibelungen hydrothermal field (8°18'S, Mid-Atlantic Ridge): Constraints on
944 fluid-rock interaction in heterogeneous lithosphere. Chemical Geology, 280, 1-18.
945 Schmidt, K., Koschinsky, A., Garbe, S. D., de Carvalho, L. M., and Seifert, R. (2007)
946 Geochemistry of hydrothermal fluids from the ultramafic-hosted Logatchev
947 hydrothermal field, 15°N on the Mid-Atlantic Ridge: temporal and spatial
948 investigation. Chemical Geology, 242, 1-21.

949 Schrenk, M. O., Brazelton, W. J., and Lang, S. Q. (2013) Serpentinization, carbon, and
950 deep life. Reviews in Mineralogy and Geochemistry, 75, 575-606.
951 Schwarzenbach, E. M., Früh-Green, G. L., Bernasconi, S. M., Alt, J. C., and Plas, A.
952 (2013) Serpentinization and carbon sequestration: A study of two ancient
953 peridotite-hosted hydrothermal systems. Chemical Geology, 351, 115-133.
954 Seewald, J. S., Zolotov, M. Y., and McCollom, T. (2006) Experimental investigation of
955 single carbon compounds under hydrothermal conditions. Geochimica et
956 Cosmochimica Acta, 70, 446-460.
957 Seyfried, W. E., and Dibble, W. E. J. (1980) Seawater-peridotite interaction at 300 °C
958 and 500 bars: implications for the origin of oceanic serpentinites. Geochimica et
959 Cosmochimica Acta, 44, 309-321.
960 Seyfried, W. E., Jr., Foustoukos, D. I., and Fu, Q. (2007) Redox evolution and mass
961 transfer during serpentinization; an experimental and theoretical study at 200 °C,
962 500 bar with implications for ultramafic-hosted hydrothermal systems at mid-
963 ocean ridges. Geochimica et Cosmochimica Acta, 71, 3872-3886.
964 Seyfried, W. E., Jr., Gordon, P. C., and Dickson, F. W. (1979) A new reaction cell for
965 hydrothermal solution equipment. American Mineralogist, 64, 646-649.
966 Seyfried, W. E., Pester, N. J., Ding, K., and Rough, M. (2011) Vent fluid chemistry of the
967 Rainbow hydrothermal system (36˚N, MAR): Phase equilibria and in situ pH
968 controls on subseafloor alteration processes. Geochimica et Cosmochimica Acta,
969 75, 1574-1593.
970 Shock, E., and Canovas, P. (2010) The potential for abiotic organic synthesis and
971 biosynthesis at seafloor hydrothermal systems. Geofluids, 10, 161-192.

Sleep, N., Meibom, A., Fridriksson, T., Coleman, R., and Bird, D. (2004) H_2-rich fluids from serpentinization: Geochemical and biotic implications. Proceedings of the National Academy of Sciences, 101, 12818 - 12823.

Stesky, R. M., and Brace, W. F. (1973) Electrical conductivity of serpentinized rocks to 6 kilobars. Journal of Geophysical Research, 78, 7614-7621.

Thayer, T. P. (1966) Serpentinization considered as a constant-volume metasomatic process. American Mineralogist, 51, 685-710.

Toft, P. B., Arkani-Hamed, J., and Haggerty, S. E. (1990) The effects of serpentinization on density and magnetic susceptibility: a petrophysical model. Physics of the Earth and Planetory Interiors, 65, 137-157.

Velbel, M. A. (2014) Stoichiometric reactions describing serpentinization of anhydrous primary silicates: a critical appraisal, with application to aqueous alteration of chondrule silicates in CM carbonaceous chondrites. Clays and Clay Minerals 62, 126-136.

Wegner, W. W., and Ernst, W. G. (1983) Experimentally determined hydration and dehydration reactions rates in the system MgO-SiO_2-H_2O. American Journal of Science, 283, 151-180.

Wetzel, L. R., and Shock, E. L. (2000) Distinguishing ultramafic- from basalt-hosted submarine hydrothermal systems by comparing calculated vent fluid compositions. Journal of Geophysical Research, 105, 8319-8340.

Whitney, D. L. and Evans, B. W. (2010) Abbreviations for names of rock-forming minerals. *American Mineralogist* 95, 185-187.

Witt-Eickschen, G., Kaminsky, W., Kramm, U., and Harte, B. (1998) The Nature of Young Vein Metasomatism in the Lithosphere of the West Eifel (Germany): Geochemical and Isotopic Constraints from Composite Mantle Xenoliths from the Meerfelder Maar. Journal of Petrology, 39, 155-185.

Wogelius, R. A., and Walther, J. V. (1991) Olivine dissolution at 25°C: Effects of pH, CO_2, and organic acids. Geochimica et Cosmochimica Acta, 55, 943-954.

Wolery, T. J. (1992) EQ3NR, A Computer Program for Geochemical Aqueous Speciation-Solubility Calculations: Theoretical Manual, User's Guide, and Related Documentation (Version 7.0), Lawrence Livermore National Laboratory.

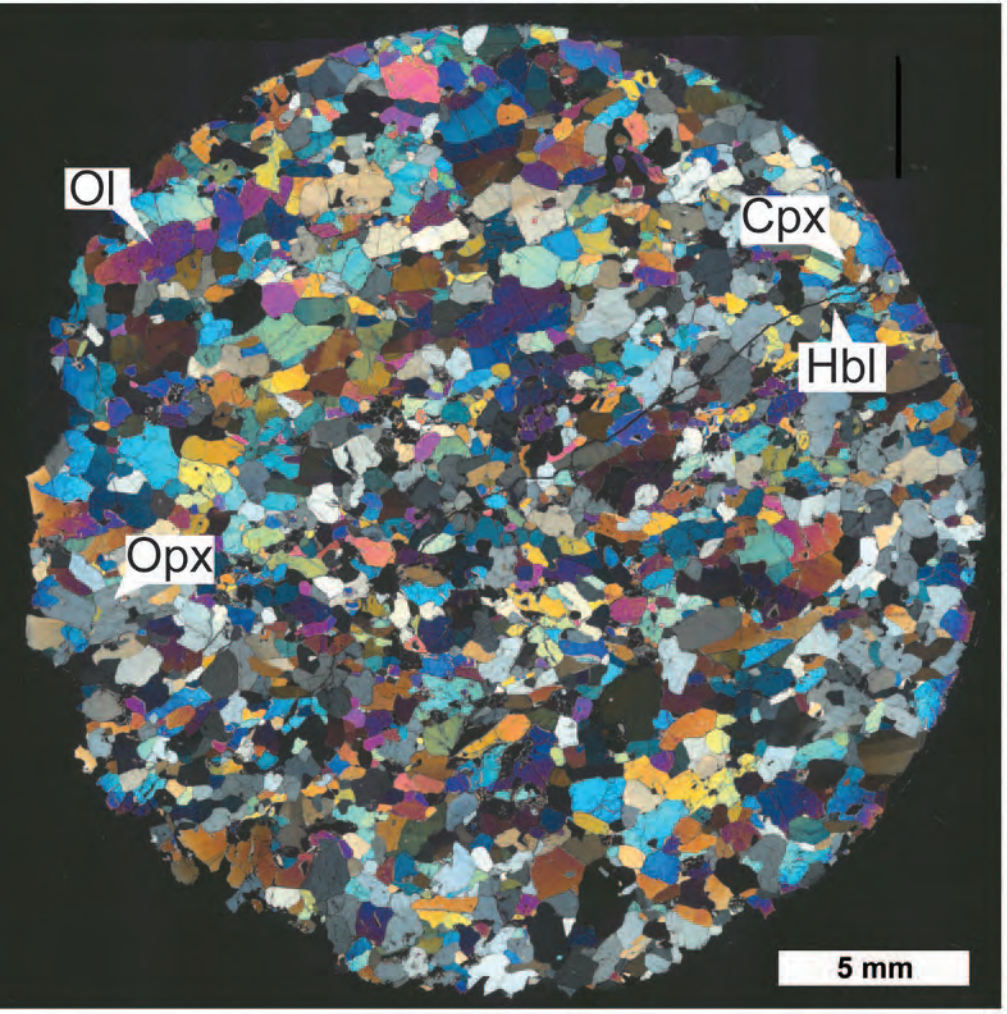

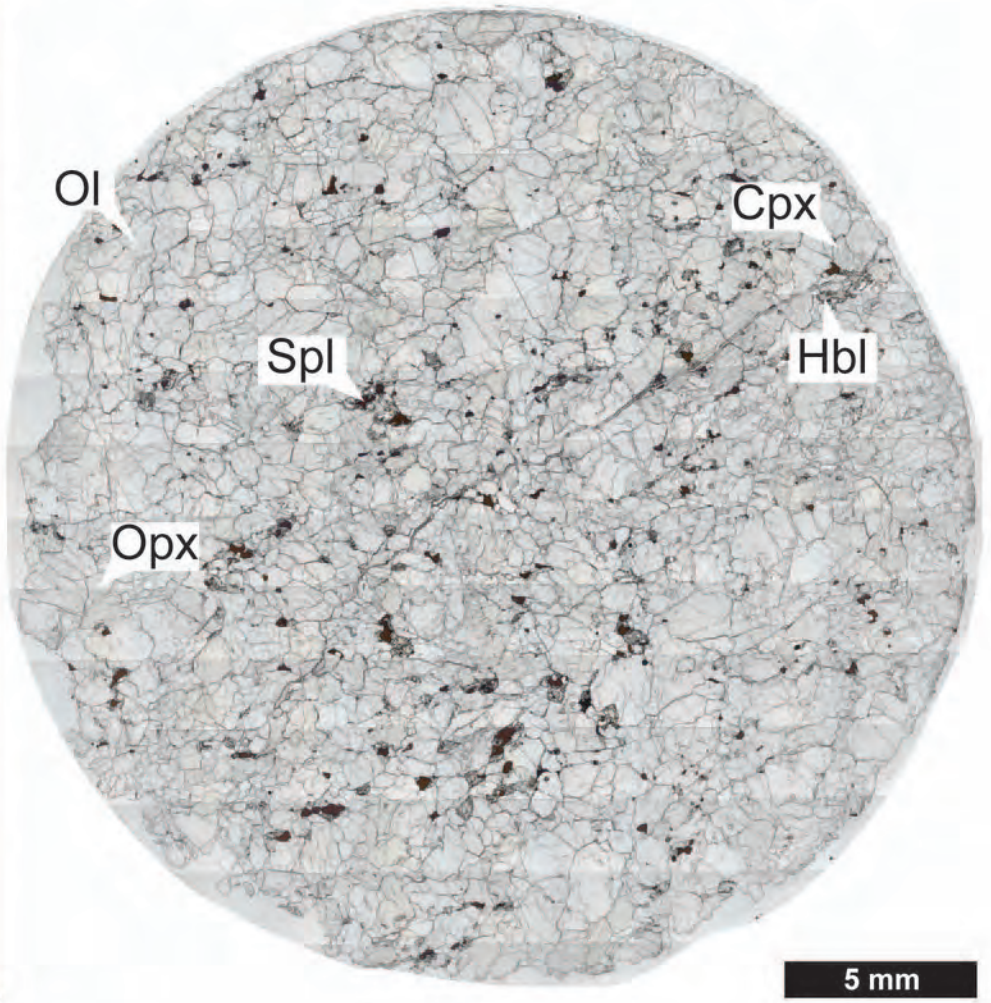

Figure 1

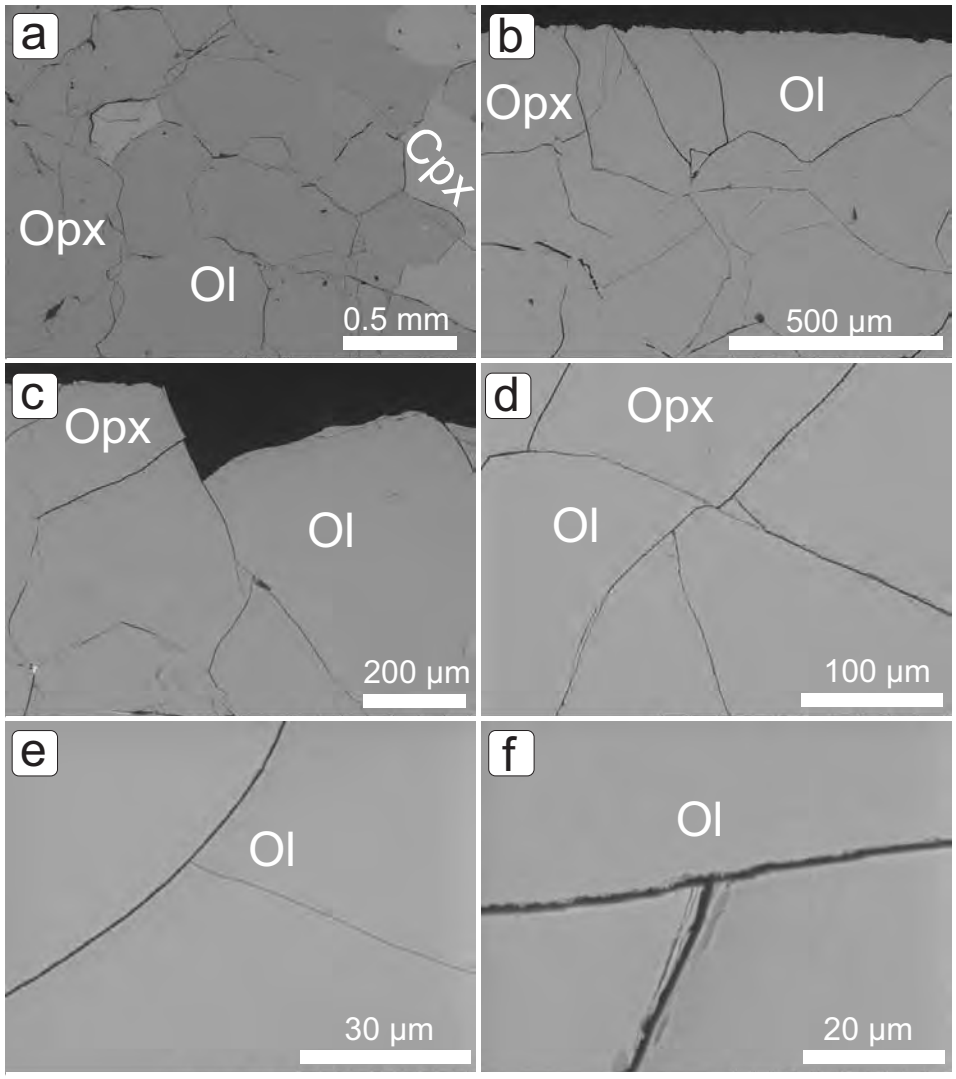
a
Cpx
Opx
Ol
0.5 mm
b
Opx
Ol
500 µm
c
Opx
Ol
200 µm
d
Opx
Ol
100 µm
e
Ol
30 µm
f
Ol
20 µm

Figure 2

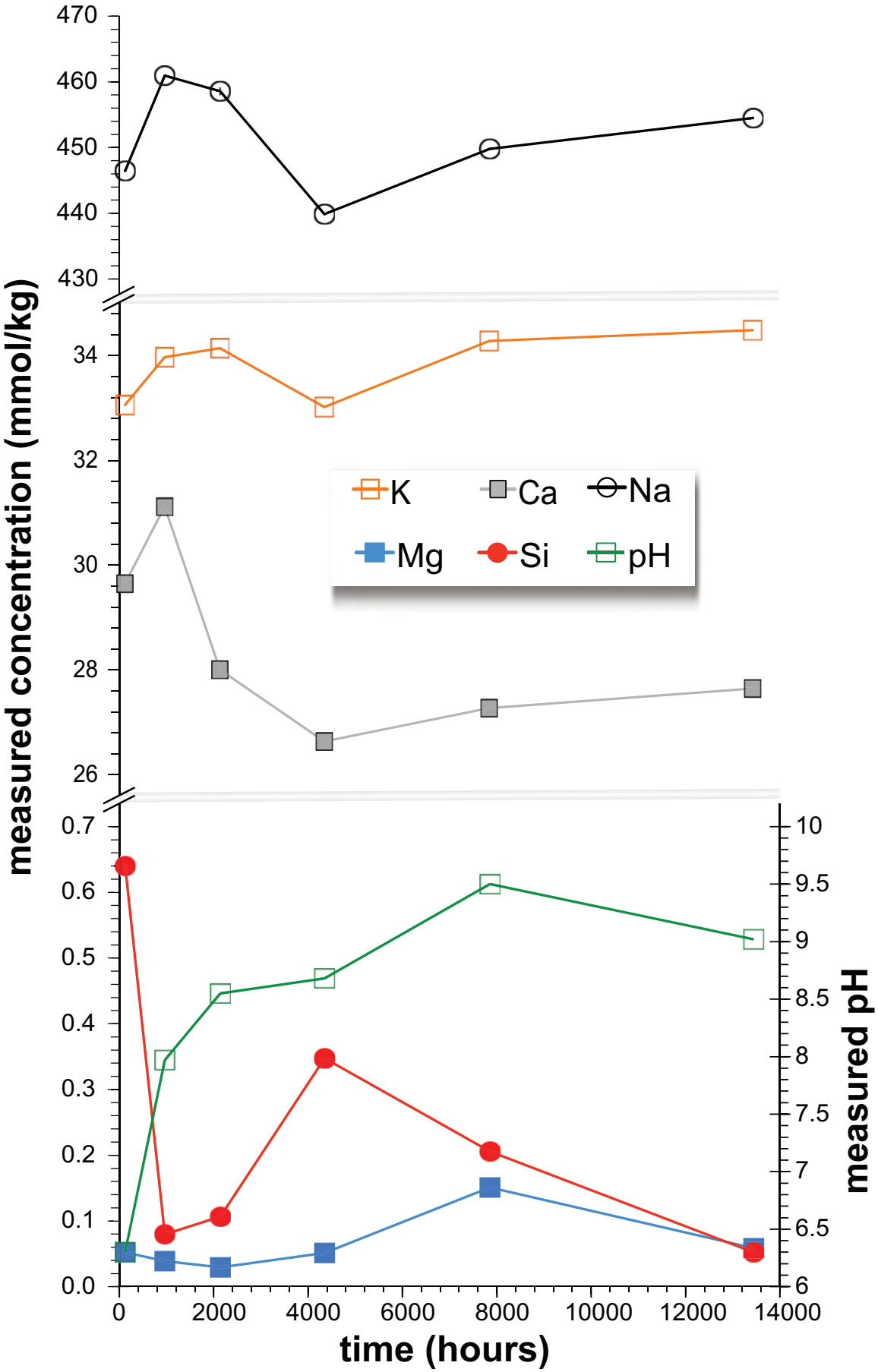
measured concentration (mmol/kg)
470
460
450
440
430
34
32
30
28
26
K
Ca
Na
Mg
Si
pH
0.7
0.6
0.5
0.4
0.3
0.2
0.1
0.0
10
9.5
9
8.5
8
7.5
7
6.5
6
measured pH
0
2000
4000
6000
8000
10000
12000
14000
time (hours)

Figure 3

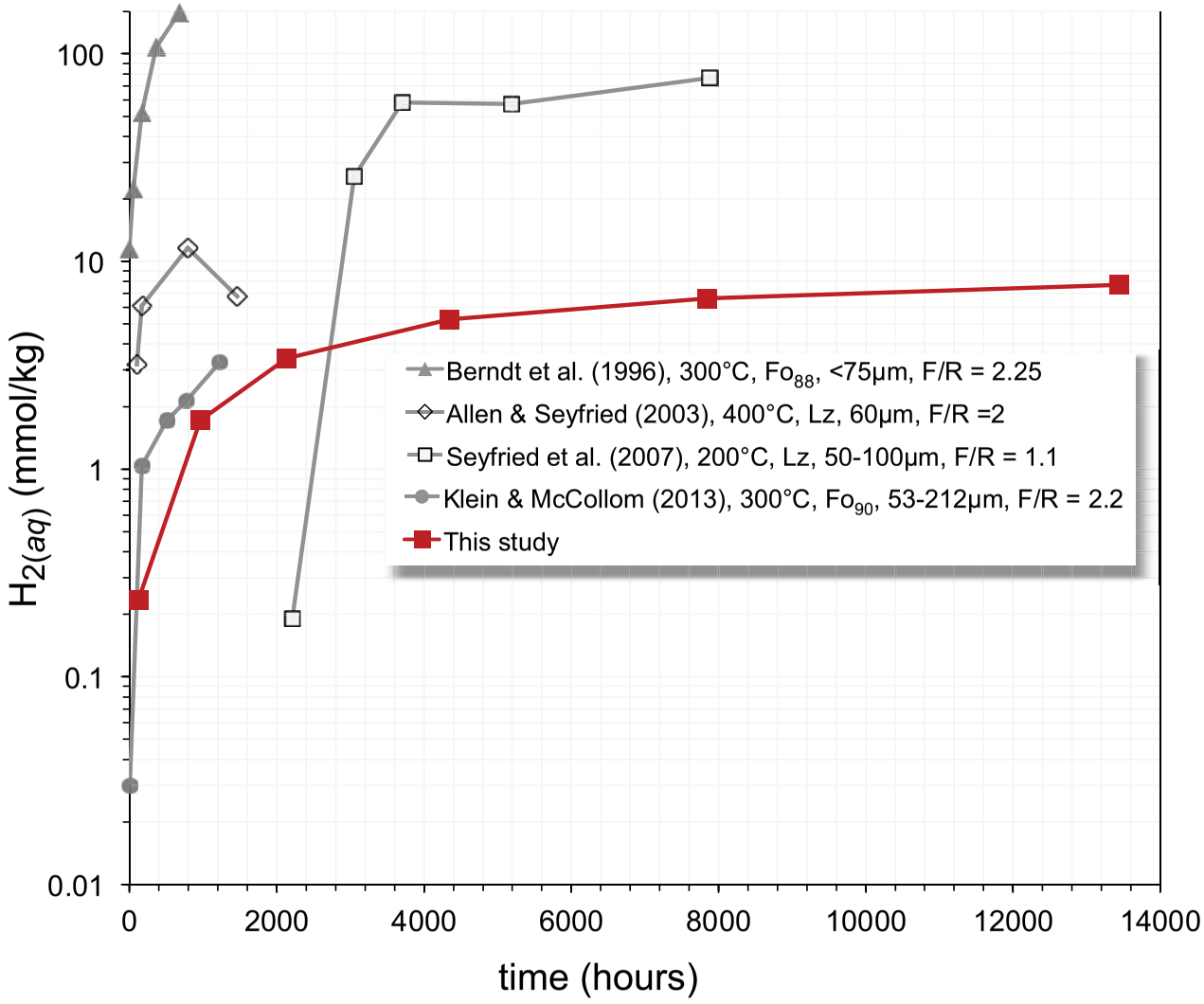
100
10
1
0.1
0.01
0
2000
4000
6000
8000
10000
12000
14000
time (hours)
H2(aq) (mmol/kg)
Berndt et al. (1996), 300°C, Fo88, <75µm, F/R = 2.25
Allen & Seyfried (2003), 400°C, Lz, 60µm, F/R =2
Seyfried et al. (2007), 200°C, Lz, 50-100µm, F/R = 1.1
Klein & McCollom (2013), 300°C, Fo90, 53-212µm, F/R = 2.2
This study

Figure 4

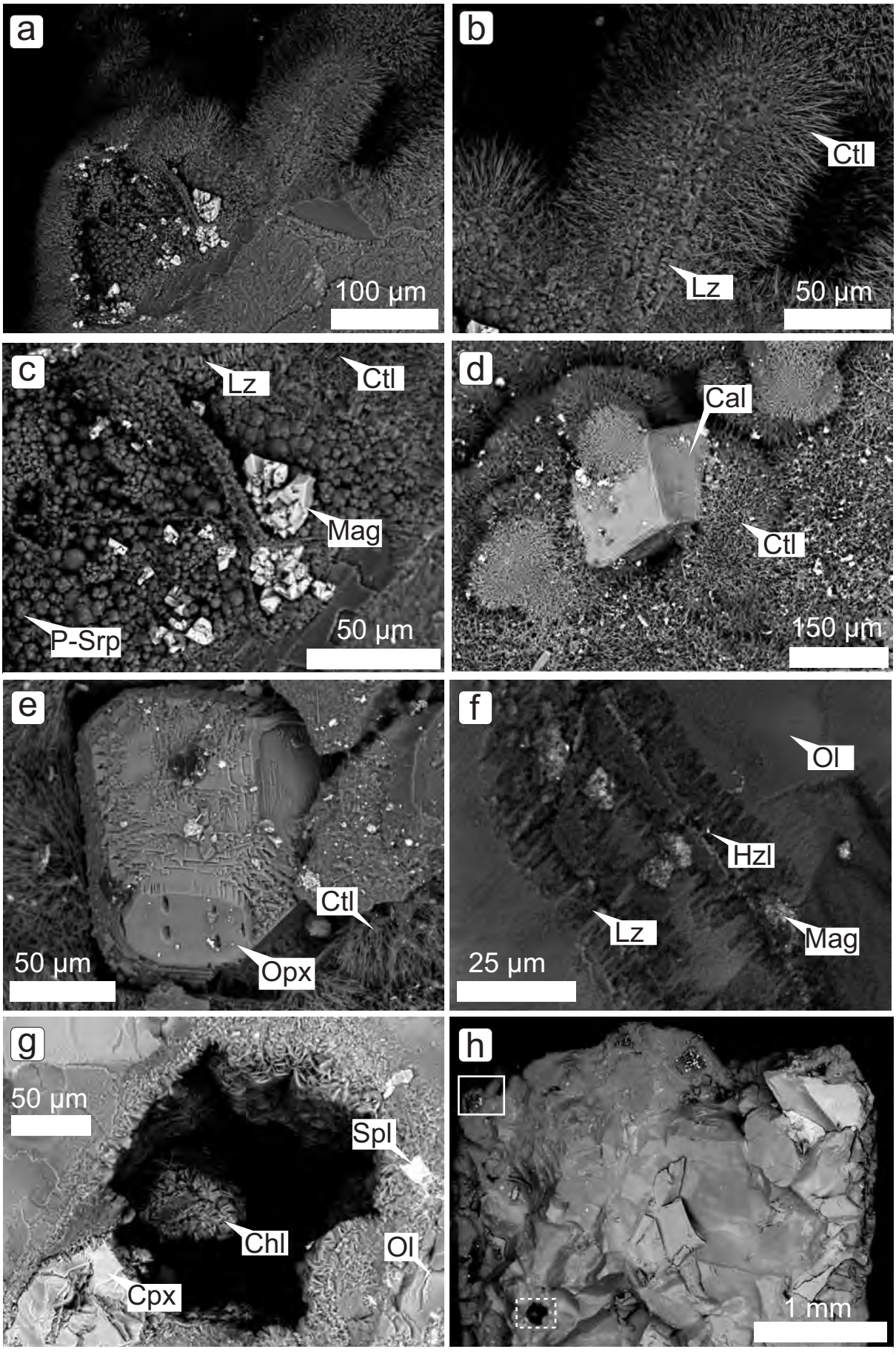
a
100 µm
b
Ctl
Lz
50 µm
c
Lz
Ctl
Mag
P-Srp
50 µm
d
Cal
Ctl
150 µm
e
Ctl
50 µm
Opx
f
Ol
Hzl
Lz
Mag
25 µm
g
50 µm
Spl
Chl
Ol
Cpx
h
1 mm

Figure 5

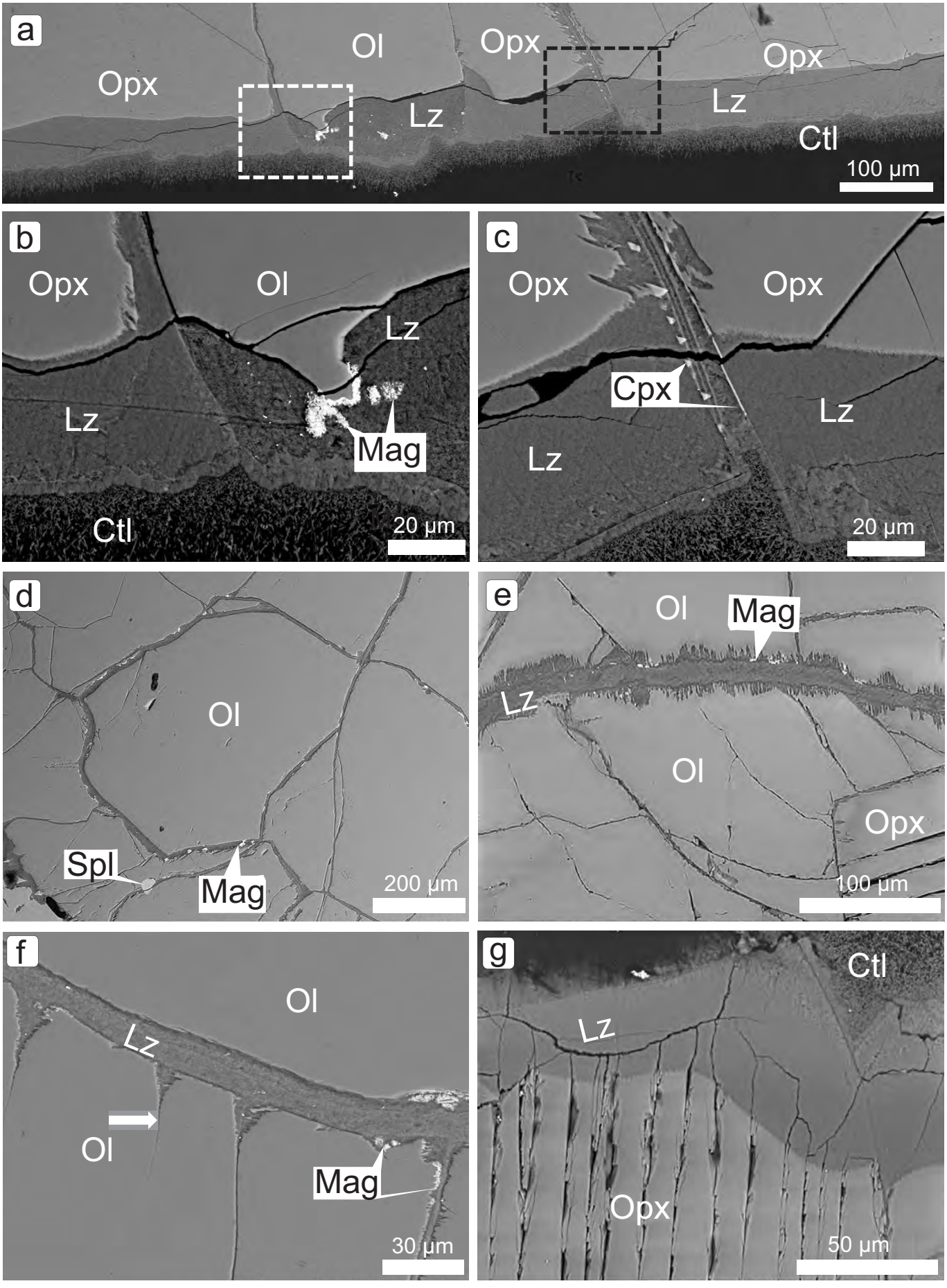
a
Opx
Ol
Opx
Opx
Lz
Lz
Ctl
100 µm
b
Opx
Ol
Lz
Lz
Mag
Ctl
20 µm
c
Opx
Opx
Cpx
Lz
Lz
20 µm
d
Ol
Spl
Mag
200 µm
e
Ol
Mag
Lz
Ol
Opx
100 µm
f
Ol
Lz
Ol
Mag
30 µm
g
Ctl
Lz
Opx
50 µm

Figure 6

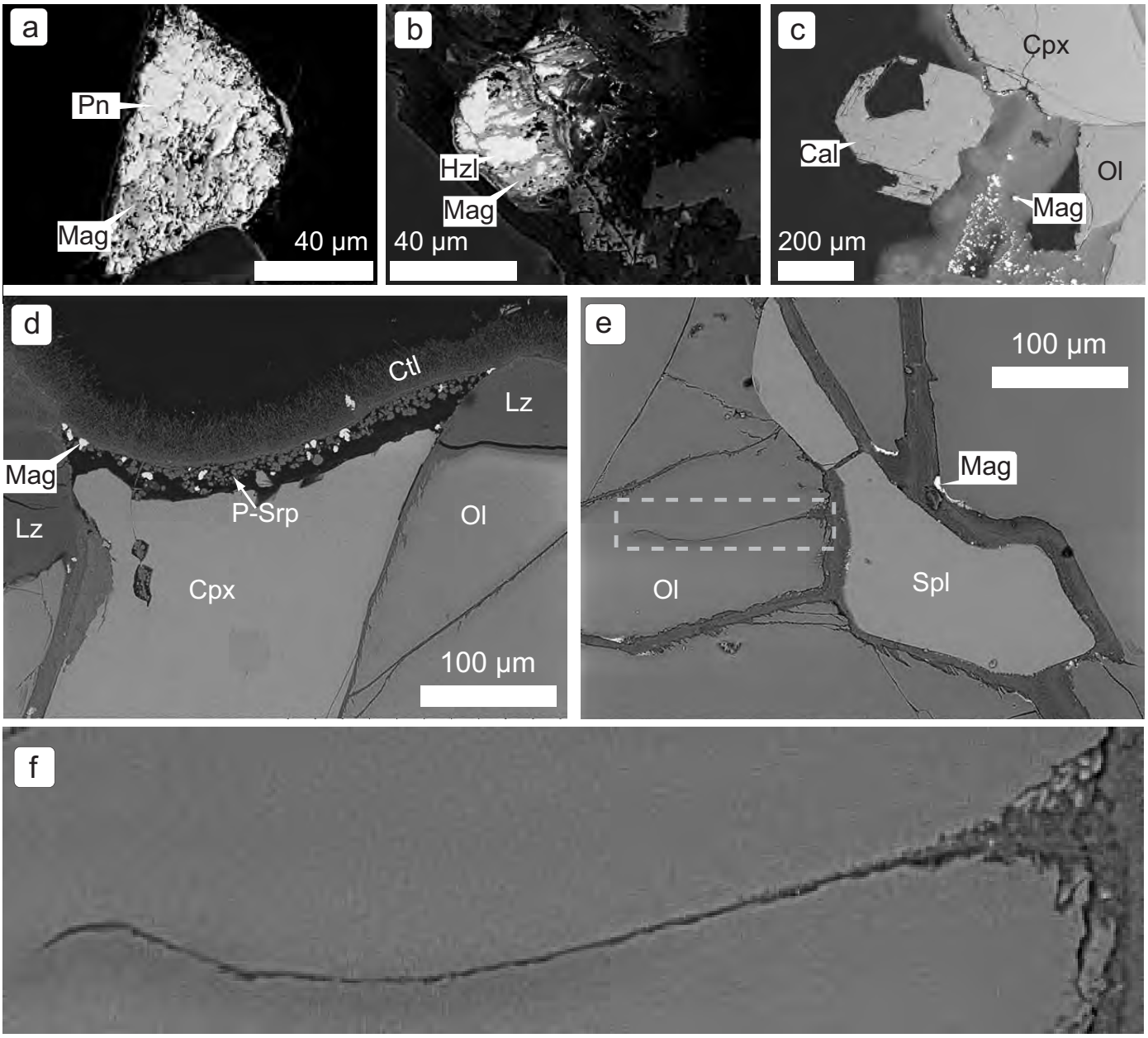
a
Pn
Mag
40 µm
b
Hzl
Mag
40 µm
c
Cpx
Cal
Ol
Mag
200 µm
d
Ctl
Lz
Mag
P-Srp
Lz
Ol
Cpx
100 µm
e
100 µm
Mag
Ol
Spl
f

Figure 7

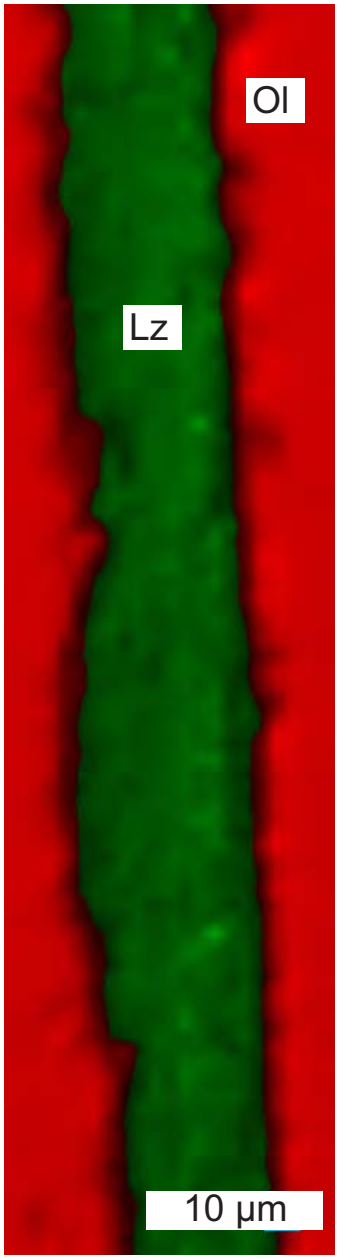

Figure 8

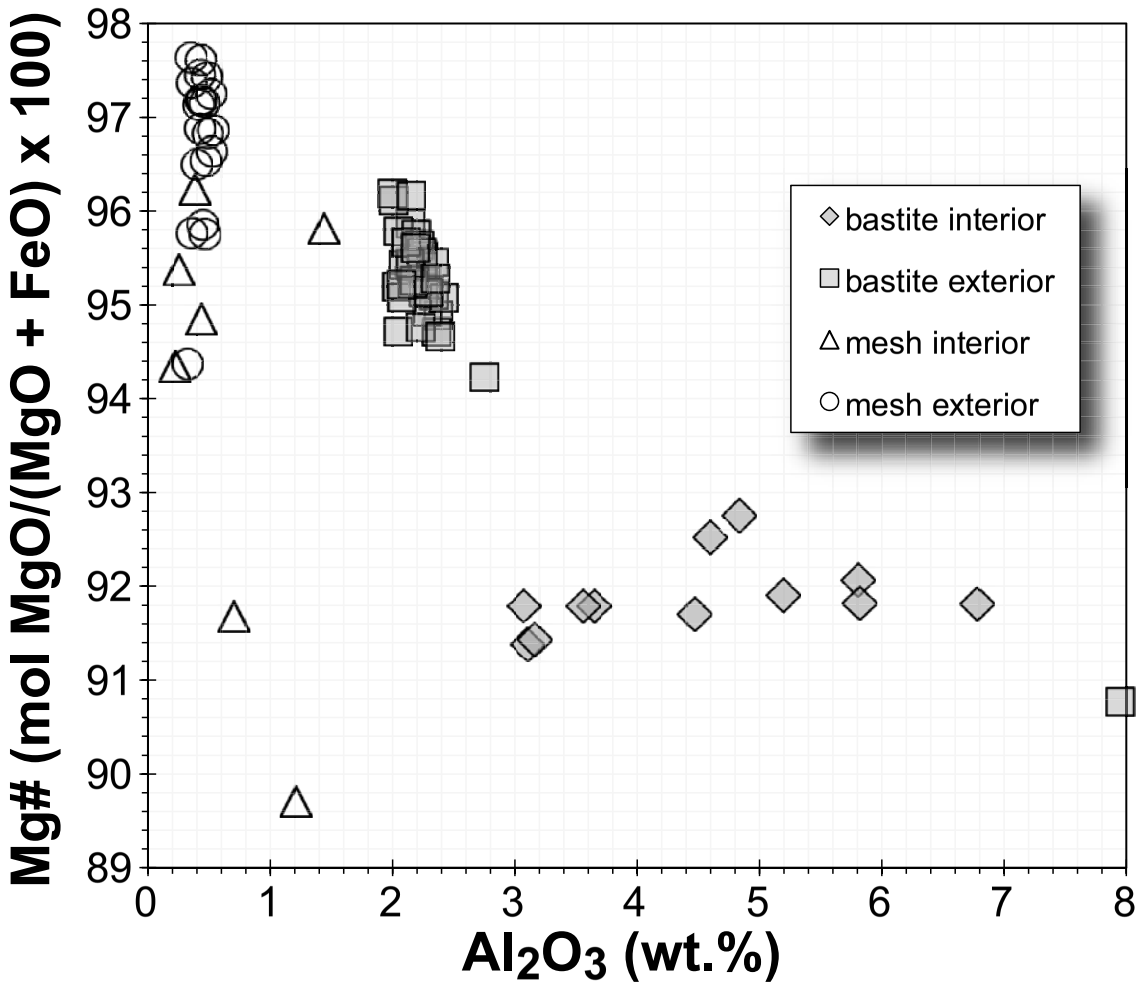
Mg# (mol MgO/(MgO + FeO) x 100)
98
97
96
95
94
93
92
91
90
89
0
1
2
3
4
5
6
7
8
Al2O3 (wt.%)
bastite interior
bastite exterior
mesh interior
mesh exterior

Figure 9

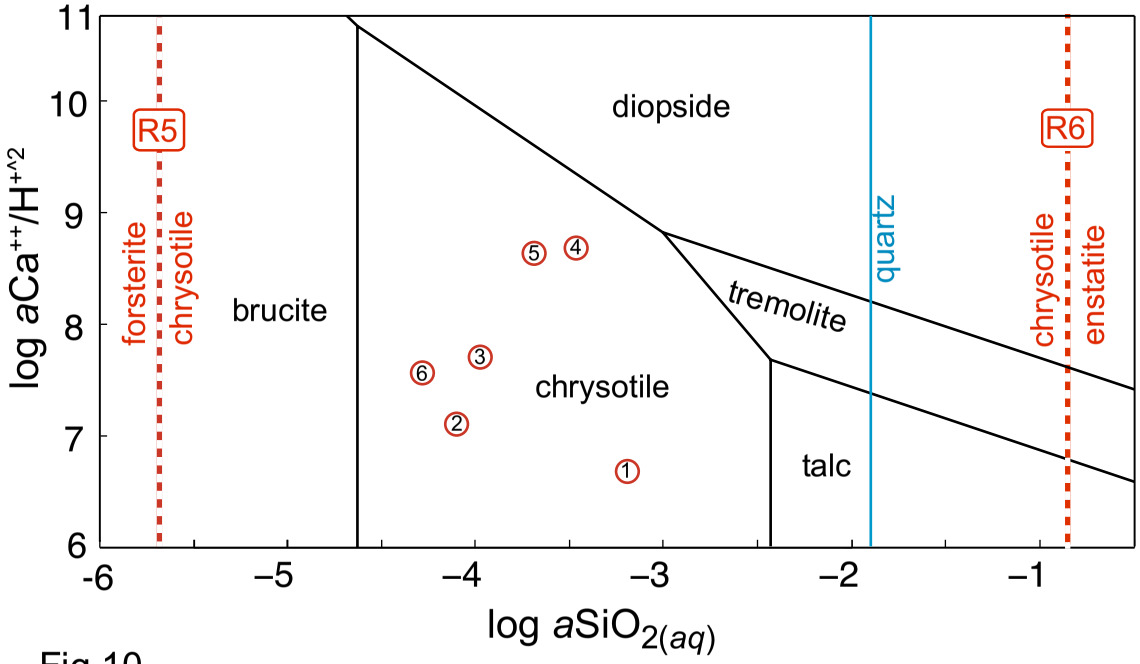
11
10
9
8
7
6
-6
−5
−4
−3
−2
−1
log aCa++/H+^2
log aSiO2(aq)
R5
R6
forsterite
chrysotile
chrysotile
enstatite
quartz
brucite
diopside
tremolite
chrysotile
talc
1
2
3
4
5
6

Fig 10

Table 1: Geochemical composition of harzburgite used as the starting material

	wt.%
SiO_2	44.66
TiO_2	0.01
Al_2O_3	1.01
FeO*	7.67
MnO	0.12
MgO	45.96
CaO	0.65
Na_2O	0.04
K_2O	b.d.
P_2O_5	0.02
Sum	100.15
selected trace elements (µg/g)	
Ni	2404
Cr	2101
V	25
Ba	6
Sr	13
Cu	11
Zn	48

*** Total Fe calculated as FeO**

Table 2: Electron microprobe analyses of primary minerals (wt.%)

	Ol	σ	Opx	σ	Cpx	σ	Amp	σ
# analyses	6		3		8		4	
SiO_2	41.13	0.29	56.76	0.29	53.49	0.53	43.46	0.09
TiO_2	0.01	0.02	0.02	0.04	0.08	0.06	0.32	0.10
Al_2O_3	0.01	0.01	2.96	0.23	3.52	0.15	14.83	0.05
Cr_2O_3	0.01	0.02	0.34	0.02	0.60	0.06	1.48	0.08
FeO	8.67	0.15	6.10	0.14	2.85	0.09	4.10	0.07
MnO	0.12	0.05	0.15	0.02	0.05	0.03	0.06	0.05
MgO	49.96	1.39	34.39	0.30	16.92	0.29	18.47	0.13
NiO	0.37	0.03	0.07	0.01	0.05	0.03	0.11	0.02
CoO	0.03	0.02	0.01	0.01	0.03	0.02	b.d.	
CaO	0.08	0.05	0.56	0.10	22.31	0.28	11.52	0.05
Na_2O	n.a.		0.04	0.01	0.86	0.03	2.89	0.01
K_2O	n.a.		b.d.		b.d.		1.09	0.00
Cl	n.a.		n.a.		n.a.		0.19	0.00
sum	100.38		101.39		100.76		98.54	

Ol = olivine, Opx = orthopyroxene, Cpx = clinopyroxene, Amp = amphibole, b.d. = below detection, n.a. = not analyzed

Table 3: Measured composition of fluid samples taken during the experiment

Sample		Time (hours)	Na (mmol/kg)	K (mmol/kg)	Ca (mmol/kg)	Mg (mmol/kg)	Si (mmol/kg)	H2 (mmol/kg)	pH	fluid (g)
starting fluid		-	463	34.0	31.1	n.d.	n.d.	n.d.	n.d.	-
bleed		0	439.6	32.4	30.5	0.03	n.d.	0.0	n.d.	43.15
	1	122	446.5	33.1	29.7	0.05	0.64	0.2	6.3	37.35
	2	963	460.9	34.0	31.1	0.04	0.08	1.7	8	34.4
	3	2138	458.6	34.1	28.0	0.03	0.11	3.4	8.6	31.01
	4	4348	439.9	33.0	26.6	0.05	0.35	5.3	8.7	27.26
	5	7850	449.8	34.3	27.3	0.15	0.21	6.6	9.5	23.17
	6	13441	454.5	34.5	27.6	0.06	0.05	7.7	9	18.34

n.d. = not determined

Table 4: Summary of petrographic observations

Primary mineral	Secondary mineral	Texture	Comments
Ol	Srp/Mag, Hzl?	mesh	Ol shows dissolution features and fractures. Intra- and transgranular veins composed of Lz, minor Mag, and traces of Hzl. Ctl and Mag after Ol are sub- to euhedral on rock exterior surface.
Opx	Srp, Chl	bastite	Opx shows etch pits, intra- and transgranular veins composed of Lz and Chl.
Spl	-	-	Spl appears unaltered.
Cpx	-	-	Cpx appears unaltered.
Po / Pn	Hzl/Mag	-	Sulfides are irregularly distributed.
Amp	Chl	-	Amp appears mostly unaltered. In some cases it appears to be replaced by Chl
-	Cal		Sub- to euhedral Cal precipitates exclusively on exterior rock surface.

Mineral and mineral group abbreviations after Whitney and Evans (2010)

Table 5: *Electron microprobe analyses of reaction products (in wt.%)*

	mesh exterior	σ	bastite exterior	σ	mesh interior	σ	bastite interior
# analyses	**10**		**36**		**4**		**7**
SiO_2	40.90	0.49	38.76	0.72	39.90	1.21	37.81
TiO_2	0.02	0.03	0.04	0.05	0.02	0.03	0.02
Al_2O_3	0.45	0.06	2.38	0.97	0.44	0.20	5.05
Cr_2O_3	0.02	0.02	0.38	0.06	0.03	0.04	0.31
$FeO^{\dagger}$	2.60	0.66	3.53	0.55	4.22	1.32	5.14
MnO	0.04	0.03	0.07	0.03	0.08	0.04	0.09
MgO	40.32	0.33	39.36	1.02	39.12	1.86	33.54
NiO	0.41	0.12	0.11	0.04	0.18	0.08	0.11
CoO	0.02	0.02	0.02	0.02	0.04	0.04	0.02
SO_3	0.08	0.03	0.04	0.02	0.06	0.03	0.11
CaO	0.07	0.02	0.17	0.02	0.11	0.05	0.37
Na_2O	0.07	0.02	0.08	0.02	0.04	0.02	0.25
K_2O	0.02	0.01	0.03	0.01	0.03	0.02	0.13
F	0.01	0.01	0.01	0.01	0.05	0.03	0.02
Cl	0.19	0.07	0.32	0.05	0.18	0.07	0.12
H_2O^*	14.78	0.68	14.71	0.65	15.51	2.36	16.92

	heazlewoodite	σ	pentlandite	σ		calcite	σ
# analyses	**5**		**4**			**7**	
Cr	0.05	0.03	0.03	0.03	MnO	b.d.	-
Mn	b.d.	-	0.01	0.01	MgO	0.04	0.02
Co	0.30	0.04	0.68	0.04	SiO_2	b.d.	-
Cu	0.10	0.02	0.19	0.03	FeO	0.02	0.02

Mg	0.05	0.01	0.04	0.01	CaO	56.54	0.40
Si	0.02	0.01	0.02	0.02	CO_2*	43.4	0.39
Ti	0.02	0.02	0.04	0.02			
Fe	3.08	0.83	28.33	0.15			
Ni	70.2	0.40	36.5	0.19			
Ca	0.02	0.01	b.d.	-			
S	26.29	0.08	32.59	0.29			
Pt	0.01	0.01	0.01	0.01			
P	0.01	0.01	0.01	0.01			
Sum	100.15	0.49	98.45	0.53			

† total Fe calculated as FeO, *calculated by difference, b.d. = below detection limit

σ	chlorite 3	σ
1.23	34.73	1.14
0.03	0.15	0.14
1.01	10.93	0.61
0.23	0.03	0.03
0.24	6.53	0.26
0.02	0.12	0.06
0.61	32.14	0.65
0.05	0.14	0.01
0.03	0.06	0.05
0.03	0.03	0.02
0.16	0.16	0.02
0.17	0.08	0.03
0.06	0.30	0.31
0.04	0.02	0.03
0.05	0.22	0.07
1.42	14.36	1.52